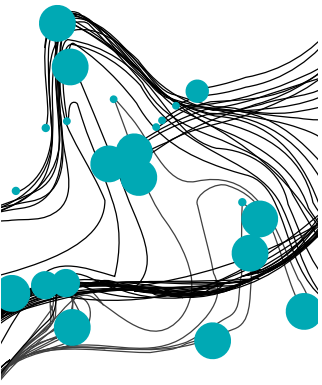
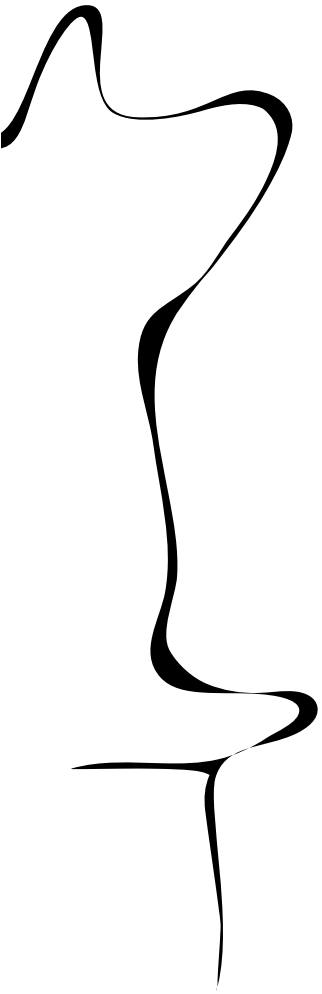


RAM ROBOTICS AND MECHATRONICS



MR-SAFE 3D-PRINTABLE FORCE SENSORS

A.J.H. (Antonie) Veldwachter

MSC ASSIGNMENT

Committee:
prof. dr. ir. S. Stramigioli
dr. V. Groenhuis, MSc
dr. ir. W.M. Brink

May, 2026

023RaM2026
Robotics and Mechatronics
EEMCS
University of Twente
P.O. Box 217
7500 AE Enschede
The Netherlands



UNIVERSITY OF TWENTE. | TECHMED CENTRE
UNIVERSITY OF TWENTE. | DIGITAL SOCIETY INSTITUTE

Summary

MRI-guided robotics is gaining interest in the robotics community. Robotic systems are used in minimally invasive procedures such as biopsies. However, current workflows remain time-intensive, as imaging and intervention must be performed in alternating cycles. During a biopsy, this repetitive process results in procedure times of approximately one hour.

Existing MRI-guided robotic systems aim to streamline this workflow but remain limited in performance. These systems rely solely on MRI screenings for positional feedback and lack force feedback at the needle tip. As a result, they suffer from slow localisation and positioning errors. Stakeholders specifically identify errors during tissue interaction; external forces acting on the needle influence the behaviour of the robotically controlled manipulators (RCMs) in ways the system cannot currently detect or compensate for.

This project addresses this limitation by introducing force and torque sensing at the end effector. The mission of this work is:

Design MR-safe sensors to measure axial force and torques at the end effector.

Force sensing at the needle tip is expected to improve safety, reliability, and spatial awareness of surrounding tissue. Three degrees of freedom are considered: axial force, yaw and pitch torques, as these represent the dominant interactions during needle insertion.

The sensing challenge is significant as MRI environments restrict the use of metallic and conductive materials near the scanner bore, eliminating most conventional force-sensing technologies. This study explores two MR-safe 3D-printable sensing principles. The ATLAS method estimates force through the displacement of 3D-printed spring elements. The AEOLUS method estimates force through airflow modulation in a pneumatic chamber. A validation framework was developed to benchmark both principles under controlled and comparable conditions. Single-degree-of-freedom proof-of-concept prototypes were built and evaluated before extending each concept to a three-degree-of-freedom design.

The 3 DoF ATLAS sensor showed the most promising results. It has an axial force operating range up to 22.5 N and a torque range up to 0.45 Nm, 150% of the target range, within a ± 5 mm displacement range. Within these ranges, it achieved an accuracy of ± 1 N, falling short of the predefined requirement of ± 0.15 N. The primary limitation is hysteresis averaging 0.25 mm, caused by friction in the cable transmission of the Ferris wheel displacement measurement mechanism. This is a solvable mechanical problem, and reducing it is the most direct path to improved accuracy. However, integration tests on the MAMRI robotic arm demonstrated that the sensor in its current form already provides meaningful force feedback. Relative force variation may be sufficient to support the functional goals of spatial awareness and tissue differentiation. An interactive demonstration setup was created to display this sensors functionality through real-time force feedback and a game.

The AEOLUS concept showed promising behaviour in the 1 DoF configuration but was not scalable to a 3 DoF design. The smaller air chambers resulted in significant air consumption (340 L/min). This highlights the challenges of pneumatic sensing methods. However, it carries the benefit of leveraging existing pneumatic infrastructure, as most MRI-guided systems use pneumatic actuators.

In conclusion, this work demonstrates that MR-safe force and torque sensing at the end effector is feasible using simple, predominantly 3D-printable principles. The ATLAS concept provides a strong foundation for further optimisation and integration into MRI-guided robotic systems, where improved feedback can enhance both safety and spatial awareness.

Contents

1 Introduction **1**
1.1 Context . . . 1
1.2 Mission Statement . . . 1
1.3 Goals . . . 1

2 Background **2**
2.1 MRI scanning and interference . . . 2
2.2 MRI guided Biopsies with RCMs . . . 3
2.3 Force Sensing . . . 4

3 Analysis **6**
3.1 Stakeholder Desires . . . 6
3.2 Force Sensing benefits . . . 6
3.3 Important forces . . . 7
3.4 Required Accuracy and Range . . . 7
3.5 Project Boundaries . . . 8
3.6 System Requirements . . . 9

4 Design **11**
4.1 Validation Framework . . . 11
4.2 ATLAS . . . 13
4.3 AEOLUS . . . 20

5 Tests **24**
5.1 ATLAS Spring Materials . . . 24
5.2 ATLAS 3 DoF Functionality Test . . . 26
5.3 ATLAS 3 DoF Hysteresis Tests . . . 29
5.4 ATLAS 3 DoF Drift Test . . . 31
5.5 ATLAS 3 DoF Integration Test . . . 32
5.6 AEOLUS 1 DoF Sensor . . . 34
5.7 AEOLUS 3 DoF Sensor . . . 36

6 Discussion **38**
6.1 Requirements reflection . . . 38
6.2 AEOLUS failure analysis . . . 38
6.3 Sensor comparison . . . 39

7 Conclusions and Recommendations **41**

7.1 Conclusions . . . 41
7.2 Recommendations . . . 42

A Demo Manual **43**
A.1 Standard Use . . . 43
A.2 Common Errors . . . 44
A.3 Electrical circuit . . . 44

B Pass/Fail Summary **45**

C The 1 DoF ATLAS **46**
C.1 Description . . . 46
C.2 Tests . . . 48

D The 3 DoF ATLAS **52**
D.1 Description . . . 52
D.2 Calibration . . . 52
D.3 Tests . . . 52
D.4 Data Sheet . . . 60

E The 1 DoF AEOLUS **61**
E.1 Description . . . 61
E.2 Force to Output Voltage Test . . . 62

F The 3 DoF AEOLUS **64**
F.1 Description . . . 64
F.2 Air Usage Tests . . . 64

G POSEIDON **66**
G.1 Description . . . 66
G.2 Result and Conclusion . . . 66

H Stakeholder Interview **67**
H.1 Indicators for Needle-Tumour Contact . . . 67
H.2 Misclassification of Tissue . . . 67
H.3 Desired Additional System Data . . . 67
H.4 Failures and Mitigation . . . 67
H.5 Overall Feedback . . . 68

References **69**

1 Introduction

1.1 Context

MRI-guided robotics is gaining interest within the Robotics community (Medical, 2024; Robotics and Mechatronics (RaM), University of Twente, 2025). These systems pose a challenge by limiting the use of materials that can interfere with MRI screenings or pose a risk to the patient, such as ferromagnetic or conductive materials. Systems classified as MR-safe pose no safety risk in the MR environment. Most traditional sensors and actuators use metallic and/or conductive components and cannot be used within MR environments. MR-safe Remote Controlled Manipulators (RCMs), such as the Soteria, developed special air-guided actuators to position a needle holder into the correct orientation through MRI guidance (Bomers et al., 2017). However, MR Imaging as feedback is slow, resulting in unreliable behaviour. Increased spatial awareness could improve reliability and reduce operating time.

A biopsy needle (holder) may experience three types of force. The dominant force is the axial needle insertion force. The needle can also be pushed from the side, resulting in a torque on the connection point (yaw and pitch). These torques affect accuracy, tissue interaction, and safety, yet are currently neglected.

To address this, the project focuses on developing modular *MR-Safe* force and torque sensors for the end effector (a needle and/or its holder). Focusing on the three most dominant forces at the end effector:

- Axial force (forward/backwards resistance),
- Yaw torque (side-to-side loading),
- Pitch torque (up-down loading).

Introducing these sensors to an MRI-guided robotic system will benefit the overall safety, reliability, and spatial awareness of the system.

1.2 Mission Statement

Design MR-Safe sensors to measure axial force and torques at the end effector.

1.3 Goals

The project focuses on needle-level force sensing and transduction within MRI-guided robotic systems. The primary application considered is biopsy procedures, as this is the most common performed operation in MRI environments at this time (UMC, 2025). However, the project maintains a level of abstraction to allow applicability to future systems that may extend beyond the biopsy use case. The central objective is to design modular MR-safe sensor concepts. While these sensors could later be integrated into robotic joints and larger systems, this project will prioritise the needle interface in three degrees of freedom. The project is structured into the following sub-goals:

1. **Validation Framework:** A setup enabling the application of forces and torques for reliable sensor benchmarking and testing.
2. **Single Degree of Freedom Sensor Design:** Develop MR-safe sensor proofs-of-concept to evaluate different sensing principles.
3. **Three Degree of Freedom Sensor Design:** MR-safe sensors capable of capturing axial force, yaw, and pitch torques.
4. **Indication:** A method that presents sensor data in real time.
5. **Integration:** Demonstrate how the developed force sensors could be integrated into future MRI-guided robotic systems.

2 Background

This chapter provides relevant background for the study. Since the project focuses on MR-safe sensing and actuation, methods relying on magnetic components or electromagnetic coupling are excluded. Instead, emphasis is placed on MR-conditional and MR-safe force-sensing approaches. Additionally, relevant background information is given to create a global understanding of the topic.

2.1 MRI scanning and interference

Magnetic Resonance Imaging (MRI) operates by exploiting the alignment and relaxation behaviour of hydrogen nuclei in a strong magnetic field. To do this, it uses strong magnetic fields and radio waves. The scanner generates a static magnetic field within the bore, which aligns the nuclear spins of hydrogen atoms in the body. Radio-frequency pulses are then applied at the resonance frequency of these nuclei, perturbing their alignment. When the pulse is removed, the nuclei relax back to equilibrium, releasing energy that is detected by receiver coils placed on the body. (UMC, 2025)

As the MRI relies on magnetic fields, any material disrupting these fields interferes with the screening. Within MRI environments, three standardised safety classifications define how close a device or system may operate relative to the MRI scanner: *MR-Safe*, *MR-Conditional*, and *MR-Unsafe* International Society for Magnetic Resonance in Medicine, 2025.

MR-Safe items pose no safety hazards in the MR environment. They contain no metallic or conductive materials and do not interfere with the magnetic, gradient, or radio-frequency (RF) fields. Such items can be placed anywhere in the MRI environment without restriction.

MR-Conditional items may contain metallic or conductive materials, but can be safely used under specific conditions defined by the manufacturer. These conditions typically include limits on magnetic field strength, maximum spatial field gradient, RF exposure (SAR), and other operational parameters. Devices classified as MR-Conditional must only be used if these specified conditions are met.

MR-Unsafe items, in contrast, must never enter the MRI environment, as they can pose risks such as attraction to the magnet, excessive heating, or interference with imaging.

2.2 MRI guided Biopsies with RCMs

One of the most common MRI-guided interventions is taking a biopsy. Here is a sample of a tumour taken for further investigation. The standard biopsy is performed under ultrasound guidance. When the surrounding tissue is too dense, the tumour has similar echogenicity to the surrounding tissue, or when the tumour is located too deep within the body, ultrasound is not an effective screening modality. With modern technology, it is becoming more typical to perform these operations under more reliable MRI guidance. (Leest et al., 2019)

Traditionally, MRI-guided biopsies are performed in a manual iterative workflow. The patient is scanned to identify the target location. Secondly, the doctor must enter the MRI area to perform the biopsy. The delay between screening and insertion introduces insecurity of tumour position. To address this insecurity, the biopsy is taken multiple times in a repetitive process (screening, insertion, repeat). As a result, conventional in-bore MRI-guided biopsies are time-intensive, typically taking between 30 and 60 minutes depending on the number of required corrections and samples. (UNC Health Johnston, 2023)

Remote-controlled manipulators (RCMs) aim to improve this workflow by enabling precise needle positioning without leaving the MRI operator's room. This is achieved by positioning an MR-safe needle guide. Theoretically, this would improve the chance of a correct biopsy and operation time.

An example in MRI-guided prostate biopsy is the Soteria RCM, shown in Figure 2.1 (Bomers et al., 2017). This MR-compatible manipulator allows the operator to target prostate lesions under MR imaging by guiding a needle to the designated location.

On September 12 2025, the Soteria system was evaluated at ZGT Hospital in Hengelo. Interviews with medical personnel involved in operating the system are included in Appendix H. A key finding is that the introduction of Soteria has not led to a significant reduction in procedure time. The primary limitation identified relates to positioning accuracy. Specifically, the system's feed-forward controller lacks repeatability, producing varying outcomes for identical inputs. This issue becomes particularly pronounced during interactions with patient tissue, where medical staff report inconsistent system behaviour.

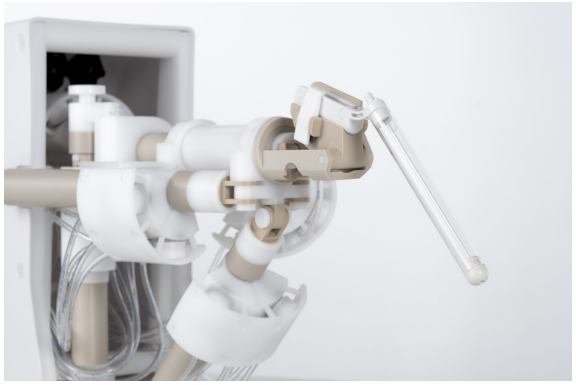


Figure 2.1: The Soteria System

2.2.1 The MAMRI

The Manipulator Arm for MRI (MAMRI), developed within the work of Groenhuis (2025), is a multi-degree-of-freedom robotic system designed to assist in MRI-guided interventions such as needle placement. Unlike earlier task-specific systems, MAMRI is conceived as a more general-purpose manipulator, capable of positioning instruments throughout the MRI bore with a relatively large workspace and high dexterity. To ensure compatibility with the MRI environment, the robot is primarily constructed from MR-safe materials.

The system employs pneumatic stepper motors, which enable actuation using pressurised air without introducing electromagnetic interference. Control and signal processing are performed outside the MRI environment, while mechanical power and sensing are transmitted to and from the robot. Although this architecture enables safe operation within the scanner, it introduces challenges related to compliance, system complexity, and sensing. In particular, interaction forces at the end effector remain unmeasured, motivating further research into MR-safe sensing solutions within systems such as MAMRI.

2.3 Force Sensing

Direct measurement of force is challenging. Instead, sensors measure secondary effects such as deformation or strain. Most conventional force-sensing technologies rely on electrical or magnetic transduction principles, which limit their applicability in MRI environments. Nevertheless, the underlying physical relationships between force and measurable effects remain valid and form the basis for MR-safe sensing strategies.

In general, force-sensing methods relevant to this work can be interpreted through two key principles: estimating force from mechanical deformation, and transducing this deformation into a measurable signal using MR-safe means. These principles are reflected in both conventional and MRI-adapted sensing approaches.

2.3.1 Force Estimation through Deformation

A common approach to force sensing is based on the relationship between applied force and resulting displacement. This is described by Hooke's law, where force is proportional to deformation for a known stiffness. In conventional systems, this deformation is measured using strain gauges, capacitive sensors, or magnetic encoders.

Although these sensing technologies themselves are not suitable for MRI environments due to their reliance on conductive or magnetic components, the principle of displacement-based force estimation remains highly relevant. If deformation can be measured using MR-safe methods, this approach provides a direct and physically interpretable pathway for force sensing.

This principle is also used in MRI-conditional research. For example, Räuber et al. (2025) measured strain in aluminium beams to estimate force, while He et al. (2024) used a spring-encoder mechanism to derive torque from rotational displacement. These approaches demonstrate the effectiveness of deformation-based sensing. Still, their reliance on conventional metallic springs limits their applicability near the MRI bore.

2.3.2 Optical Transduction Methods

Optical sensing methods provide an alternative means of measuring deformation without introducing electromagnetic interference. These methods rely on detecting changes in light properties, such as intensity, wavelength, or interference patterns, caused by mechanical strain.

A well-established example is Fibre Bragg Grating (FBG) sensing, where strain induces a shift in the reflected wavelength of light propagating through an optical fibre. This principle has been successfully applied in MRI environments by Moerman et al. (2013).

Optical methods are suitable for MRI applications due to the non-conductive and non-magnetic nature of optical fibres. However, they require external interrogation systems and precise optical alignment, which increases system complexity. This makes the overall system large and hard to integrate into an MRI-guided robotic system such as the MAMRI.

2.3.3 Fluid-Based Transduction Methods

An alternative class of MR-compatible force sensing approaches relies on fluid-based transmission of mechanical effects. In these systems, applied force is converted into pressure or displacement within a fluid, which can then be measured remotely.

Pneumatic sensing, as presented by Rie (2024), infers force from pressure changes or flow resistance within an air-filled system. Similarly, hydraulic approaches, such as the system developed by Mühlenhoff, Radler and Sattel (2024), use fluid displacement between coupled cylinders to transfer force information from the point of interaction to an external measurement unit.

These methods enable physical separation between the sensing interface and the readout system, making them well-suited for MRI environments. However, they introduce trade-offs in terms of system dynamics, sensitivity, and complexity, particularly due to compressibility, fluid inertia, and sealing requirements.

2.3.4 Displacement Measurement as an Enabler

Across the discussed methods, a recurring theme is that force sensing fundamentally depends on accurate measurement of displacement or deformation. This highlights the importance of reliable position-sensing techniques that can operate within MRI constraints.

Schlabach (2025) demonstrated an MR-compatible optical encoder system, illustrating the feasibility of displacement measurement without electromagnetic interference. While current implementations do not yet achieve the resolution required for high-precision force sensing, they provide a foundation for further development.

2.3.5 Summary and Design Implications

The reviewed approaches demonstrate that force sensing in MRI environments is not limited by the physical principles of measurement, but by the constraints on how signals can be transduced and acquired. Deformation-based sensing remains the most intuitive and widely applicable method, but requires alternative transduction mechanisms and MR-safe compliant mechanisms.

Optical and fluid-based methods provide viable solutions, each with distinct advantages and limitations. Optical systems offer high sensitivity without generating interference. Both approaches, however, introduce additional system complexity.

However, these approaches differ significantly in implementation complexity, measurement principles, and performance characteristics such as sensitivity, bandwidth, and scalability. As a result, direct comparison between reported systems is challenging. These trade-offs motivate the exploration of proof-of-concept solutions, as the current state of the field does not yet allow for a clear and consistent evaluation of the different approaches.

3 Analysis

To transfer from the background study to the system design, a more detailed understanding is required. This chapter provides insights from literature, clinical observations, and stakeholder interviews and translates them into requirements and project boundaries. This chapter addresses the following research questions:

1. Which stakeholders are involved, and what do they desire?
2. What benefits does force sensing provide in MRI-guided Robotics?
3. Which forces are most relevant to measure?
4. With what precision and ranges should those forces be measured?

These questions are answered and motivated within this chapter.

3.1 Stakeholder Desires

The main stakeholders for this project are system operators, MRI-guided system engineers, and the patients interacting with the system. The priorities and desires of each group are investigated below.

3.1.1 Operators

Operators are defined as medical personnel and doctors specialised in MRI-guided biopsies. Based on the interviews described in Appendix H, they desire a system that is simple to use, intuitive, and free of unnecessary complexity. They are not interested in the precise numerical force measurement of the needle, but rather an indication of how it feels.

3.1.2 System Engineers

System engineers only integrate the force sensor when the benefits outweigh the implementation effort. System engineers desire a modular system to support rapid prototyping. They require accurate measurement to address the specific application requirements. Higher accuracy allows a wider range of applications. The system should focus on plug-and-play functionality.

3.1.3 Patients

Patients are the least involved stakeholders and primarily value safety. The presence of a force sensor is expected to enhance safety during procedures and address this concern. At the same time, the sensor must not introduce additional discomfort, such as excessive noise or an unappealing appearance.

3.2 Force Sensing benefits

In the current situation, systems such as Soteria (Bomers et al., 2017) incur positioning errors due to their reliance on manual feedback loops and human interaction. The operating environment is highly variable and unpredictable, while the system itself lacks direct sensory feedback. Instead, the only feedback is provided indirectly through the operator.

When the Soteria interacts with surrounding tissue, it experiences force. This resistance is especially sufficient when deforming tissue. When the system experiences significant friction, it skips steps. In this situation, reliability is sacrificed to improve safety, which is counterintuitive. A safe system should be reliable.

Introducing force sensing to such a system could enhance both *reliability* and *safety*. A robot that interacts with humans should constrain output force for human safety, not by limiting the maximum output, but by monitoring the output force acting on the needle tip. This way,

reliability is not sacrificed to introduce safety layers within the system. The system can detect excessive loading before damage occurs to the equipment or the patient.

Introducing more information to the system also adds gateways to more complex systems, capable of adaptive control, autonomous motion correction, or differentiating tissue types. Force sensing will increase *spatial awareness* of the system.

To summarise, adding force sensing to an MRI-guided robot will improve:

- Safety
- Reliability
- Spatial Awareness

3.3 Important forces

As hinted at in section 3.2, the most critical forces to measure are those acting directly on the needle tip. This should be the primary site of interaction with patient tissue. Interactions include the punctuation of the needle and (un)intended lateral contact. This generates an axial force along the direction of the needle, as well as torques in the yaw and pitch directions, illustrated in Figure 3.1.

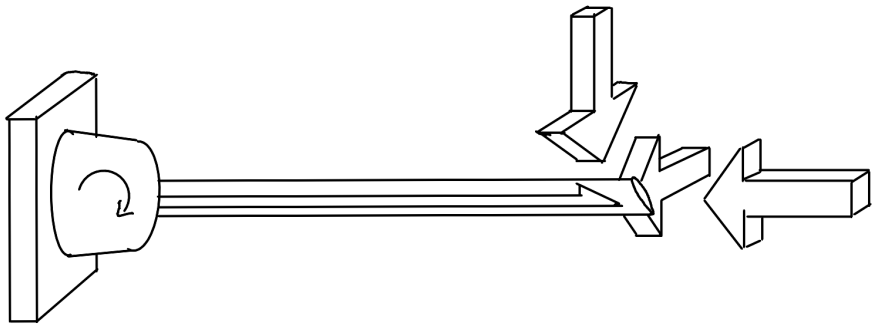


Figure 3.1: Needle Forces

Not all configurations are mounted col-linearly as shown in Figure 3.1. In some configurations, the end effector is positioned at a declined angle of $45-90°$. Under these conditions, it can be argued that all 6 degrees of freedom are relevant. However, due to the complicated nature of this project, the focus will lie on the axial force and the yaw and pitch torques.

3.4 Required Accuracy and Range

3.4.1 Axial Force

The axial force represents the dominant interaction during needle insertion. It describes skin penetration, traversal of multiple tissue layers, tumour interaction and the potential encounter of nerve interfaces. Comparable studies indicate that needle insertion force can reach values up to approximately 13 N (Ülgen, Uzun and Koçaturk, 2019; Wu et al., 2020). To ensure that the full range is captured, the operating window for the sensor is set to $[-15\,\text{N},\ 15\,\text{N}]$.

While a higher resolution is always preferable, a benchmark of 0.1 N is adopted from the study of Ülgen, Uzun and Koçaturk (2019). This provides sufficient knowledge to distinguish between tissues while remaining practical for development. Accuracy is set at $\pm 1\,\%$ of the full scale of the system, corresponding to $\pm 0.15\,\text{N}$. This balance between precision and feasibility ensures that the sensor output will be meaningful without requiring excessive complexity.

3.4.2 Required torque

Lateral force on the needle tip is smaller than the axial force. In comparable studies, forces between 1 N and 3 N were used, Lehmann et al. (2017) and Misra, Reed and Okamura (2012). The range is set at [−3 N, 3 N]. Lateral force is transferred into torque since the needle acts as a lever. The needle length currently in use for the MAMRI project is $l_{\text{needle}} \approx 0.1\,\text{m}$. Resolution is set at 0.1 N, similar to the axial force. The resulting range and resolution are.

$$\tau_{\text{base}} = l_{\text{needle}} \times F \tag{3.1}$$

$$\tau_{\text{max}} = 3\,\text{N} \times 0.1\,\text{m} = 0.3\,\text{Nm} \tag{3.2}$$

$$\tau_{\text{resolution}} = 0.1\,\text{N} \times 0.1\,\text{m} = 0.01\,\text{Nm} \tag{3.3}$$

The calculation shows the acting range for yaw and pitch torque sensing, [−0.3 Nm, 0.3 Nm]. Since the acting range is smaller, the accuracy will be ±5% of the acting range. The required accuracy is now ±0.015 Nm. These values are consistent with both the expectations from the literature and ensure that torque feedback is meaningful.

Summarising, Table 3.1 shows the found values for required precision and range.

Table 3.1: Desired Values

	Linear Force	**Torque**
Range	[−15 N, 15 N]	[−0.3 Nm, 0.3 Nm]
Resolution	0.1 N	0.01 Nm
Accuracy	±0.15 N	±0.015 Nm

3.5 Project Boundaries

Project Boundaries maintain the focus and feasibility of the study. The project scope is the design of end-effector force and torque sensors. The following boundaries are set:

- **Force prioritisation:** The development focuses on a 3-DoF sensor focusing on axial force, yaw and pitch torques. The other degrees of freedom will have minimal attention.
- **Measurement location:** All forces will be measured at the end effector, ensuring that sensor development is aligned with the intended application point.
- **Sensor focus:** The primary focus is on the development and validation of the sensors themselves. Methods for indicating or visualising forces will be implemented only for demonstration purposes and are not part of the core development.
- **Proof-of-principle objective:** The project aims to establish a proof of principle. Detailed considerations, such as hygiene cycles or full compliance with medical procedures, are outside the scope.
- **MR-safe verification:** The sensor designs are MR-safe in principle, containing no metallic or conductive components within the scanner bore. Verification in an MRI environment is considered outside the scope of this study.

3.6 System Requirements

In this context, the term *system* refers to the complete setup, including both the force/torque sensors and the indication components. The term *sensor* specifically refers to the measurement element.

3.6.1 Stakeholder Requirements

Stakeholder requirements are derived from the stakeholder desires presented in Chapter 3.1. The current project will not focus on sterilisation and disinfection cycles; it is out of scope.

Table 3.2: Stakeholder Requirements

Nr.	Requirement	Value	MoSCoW
SR01.01	The sensor must be modular to allow integration in different systems.	-	M
SR01.02	The sensor must be plug-and-play, requiring minimal setup.	-	M
SR01.03	The system must ensure patient safety.	-	M
SR01.04	The sensor must be MR-safe.	-	M
SR01.05	The system must have a digital output for easy integration	-	M
SR01.06	The sensor should reach steady state within 2 s after a step change in applied force.	< 2 s	S
SR01.07	The sensor should be enclosed and easily cleanable (medical hygiene).	-	S
SR01.08	The system should provide an intuitive display for real-time force/torque measurements.	-	S
SR01.09	The sensor should operate reliably at typical human body temperatures	$\leq 40^\circ$	S
SR01.10	The sensor won't be robust against repeated sterilisation or disinfection cycles.	-	W

3.6.2 Technical Requirements

1. Linear Force Requirements
The linear force requirements are set in Section 3.4. This includes a range between $[-15\,\text{N}, 15\,\text{N}]$ with an accuracy of $\pm 1\%$ of full scale ($\pm 0.15\,\text{N}$). For robustness, the sensor's maximum load capacity is set to 150% of 22.5 N.

Table 3.3: Linear Technical Requirements

Nr.	Requirement	Value	MoSCoW
TR01.01	The sensor must measure axial forces within the desired range.	$[-15\,\text{N}, 15\,\text{N}]$	M
TR01.02	The sensor must measure axial force with an accuracy of $\pm 1\%$ of full scale.	$\pm 0.15\,\text{N}$	M
TR01.03	The sensor must have a resolution better than 0.1 N.	$< 0.1\,\text{N}$	M
TR01.04	The sensor must tolerate forces up to 150% of full scale.	$\leq 22.5\,\text{N}$	M
TR01.05	The sensor should have a maximum total travel of ± 5 mm	± 5 mm	S

2. Rotational Torque Requirements
Rotational torque requirements are determined in Section 3.4. This is derived using a needle length of ≈ 100 mm. For robustness, the sensor's maximum load capacity will be set to 150% of 2.25 Nm.

Table 3.4: Rotational Technical Requirements

Nr.	Requirement	Value	MoSCoW
TR02.01	The sensor must measure torque in both directions within the desired range.	[−0.3 Nm, 0.3 Nm]	M
TR02.02	The sensor must measure torque with an accuracy of ±5% of full scale.	±0.015 Nm	M
TR02.03	The sensor must have a resolution better than 0.01 Nm.	< 0.01 Nm	M
TR02.04	The sensor must tolerate forces up to 150% of full scale.	≤ 0.45 Nm	M
TR02.05	The sensor should have a maximum total travel of $\pm 5^o$	±5°	S

3. General System Performance Requirements
General requirements focus on real-time applicability. A 10 Hz feedback cycle should be sufficient, comparable to other studies. Latency below 100 ms ensures that indications remain intuitive for the operator. Calibration is included to compensate for sensor drift. The general requirements also maintain modularity, with the main design focused on the MAMRI robot.

Table 3.5: General System Performance Requirements

Nr.	Requirement	Value	MoSCoW
TR03.01	The system must provide measurements with sufficient sampling frequency for real-time feedback.	≥ 5 Hz	M
TR03.02	The sensor must stay within the MAMRI end-effector circular footprint	$\phi \leq 64$ mm	M
TR03.03	The indication (display/interface) should reflect sensor data with minimal latency.	< 100 ms	S
TR03.04	The sensor should have a modular interface.	-	S
TR03.05	The system should include a straightforward calibration procedure to account for drift or setup changes.	-	S
TR03.06	The sensor could minimise cross-sensitivity between linear and torque channels (decoupled outputs).	-	C

4 Design

As motivated in the previous chapters, this study compares guiding principles through proof-of-concept designs. A validation framework was designed to compare and benchmark sensors without bias. The 1-DoF proofs of concept serve as a feasibility study. After generating a simple proof of concept, the sensing principle can be optimised into a more complex 3-DoF version.

This chapter presents the designs of the validation framework, the ATLAS sensors, and the AEOLUS sensors. ATLAS and AEOLUS represent methods for force sensing. They both have a 1-DoF proof of concept and a 3-DoF design. This chapter will explain these designs and the reasoning behind them.

A third method, POSEIDON, uses hydraulic transduction to measure force. However, this method did not generate a simple proof-of-concept version and is therefore not described in the main body of this report. A description is provided in Appendix G.

4.1 Validation Framework

The objective of the validation framework is to apply controlled forces to the sensors during tests. It must be modular, allowing different sensors to be tested with minimal effort. The setup must be capable of simulating forces up to 22.5 N, the maximum tolerable force (Requirement TR01.04).

4.1.1 Concept

To apply controlled forces, calibrated weights are used. This approach provides a direct and reliable method for generating known forces. The applied force can be determined from the mass and gravitational acceleration. Applying weight in different configurations will result in different forces. A constant gravitational pull of $9.81\,\mathrm{m/s^2}$ is assumed for the full project.

The MAMRI robot uses a modular interface to connect its end-effectors, (Groenhuis, 2025). This interface features 8 M6 bolts equally spaced on a circle. Since this robot is a main use case for the sensors, the interface is adopted for the validation framework. The main advantage of this approach is that the sensors can later be directly incorporated into robots that already use that interface.

This modularity allows the same setup to serve as a platform for both early-stage prototyping and more advanced validation experiments. A concept sketch is given in Figure 4.1.

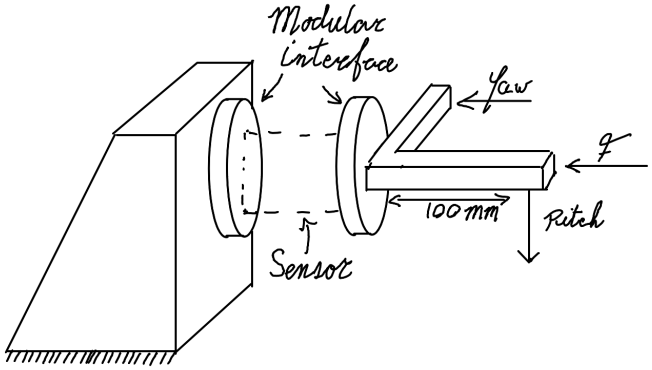


Figure 4.1: Sketch Validation Framework

4.1.2 Design

The validation framework applies controlled forces by altering the sensor position and the weight configuration. The upwards-facing setup simulates yaw torque and axial force. The forwards-facing setup simulates pitch torque.

To ensure purely axial loading, a self-centring horizontal lever is introduced and kept level during testing, preventing the introduction of unintended torques. The relation between force and weight is:

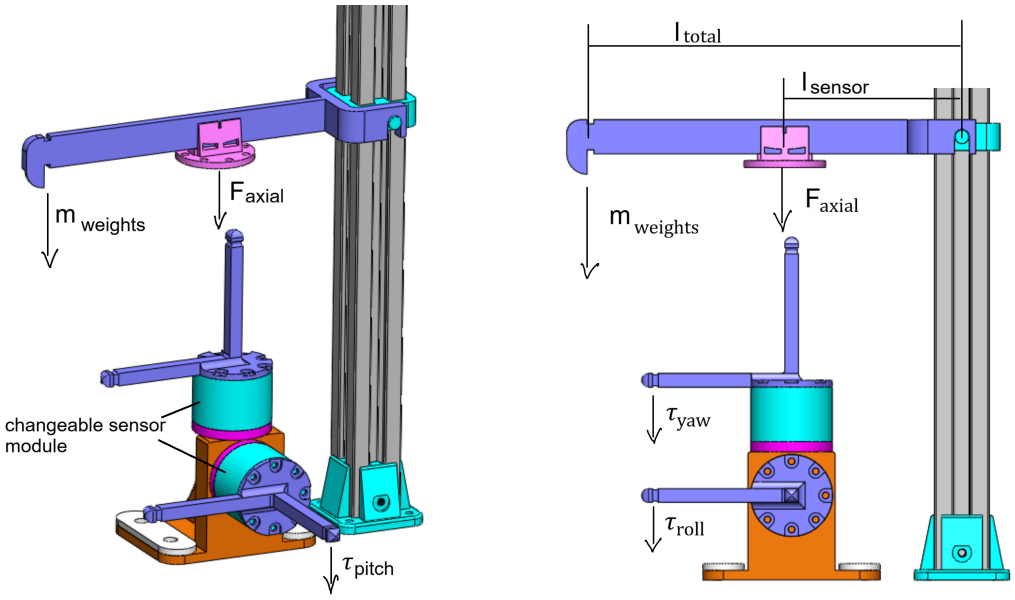
$$F_{\text{axial}} = (m_{\text{weights}} \times \frac{l_{\text{total}}}{l_{\text{sensor}}} + m_{\text{arm}}) \times g \tag{4.1}$$

To generate torque, a lever is used at the end effector. Weights can be suspended from this lever to generate torque, giving the following relation:

$$\tau_{\text{yaw/pitch}} = m_{\text{weights}} \times l_{\text{lever}} \times g \tag{4.2}$$

It should be noted that this formula assumes a force perpendicular to the lever arm. This is only true at rest when the system is horizontal. For large travel ($> 10°$), the active force component was calculated, knowing the angle of the arm. For small travel ($\leq 10°$), the effect was deemed insufficient and neglected.

The validation framework design is shown in Figure 4.2.



(a) Side View **(b)** Front View

Figure 4.2: Validation Framework

4.2 ATLAS

***A**ngular **T**orsion **L**oad **A**cquisition **S**ensor*

4.2.1 Method

The working principle of the ATLAS sensor is based on Hooke's law, which relates the force applied to a spring and its resulting displacement:

$$F = k \times x \tag{4.3}$$

In comparable studies, He et al. (2024) and Räuber et al. (2025), metallic springs are used for their low drift and large elastic range before plastic deformation. However, such materials are not MR-safe. Although MR-safe off-the-shelf spring alternatives were considered, they were deemed outside of the scope of this project. Instead, this project focuses on 3D-printed springs. This choice enables rapid prototyping and systematic variation of spring geometry and material properties. This flexibility allows the spring characteristics to be tailored to specific application requirements.

Ideal spring geometry is analytically explained in Section 4.2.2. The ideal material was found through experimentation and is explained in detail in Chapter 5.1 using the 1-DoF ATLAS concept described in Section 4.2.4. The results of this test resulted in the design of the 3-DoF ATLAS prototype described in Section 4.2.5

4.2.2 Spring Geometry

Using 3D-printed springs enables a wide variety of geometries. In addition to the choice of material, the spring geometry influences mechanical behaviour. The effective spring constant is difficult to determine through a theoretical model due to printing inconsistencies. Different printers with similar spring geometries and materials result in different spring constants.

While the spring constant should be measured for each design, the effects of geometry can be understood analytically. The 3D-printed leaf springs used can be approximated as cantilever beams. The tip deflection under an applied force F is given by

$$x = \frac{Fl^3}{3EI} \tag{4.4}$$

Here l is the spring length, E the Young's modulus of the material, and I the second moment of area of the spring cross-section. This relation shows that the deflection increases with the cube of the spring length, meaning longer springs require less force to achieve the same displacement.

Plastic deformation occurs when the bending stress at the fixed base reaches the material's yield strength. For a cantilever beam, the maximum bending stress is

$$\sigma_{\max} = \frac{Flc}{I}, \tag{4.5}$$

Combining these relations gives the maximum elastic displacement before plastic deformation:

$$x_{\max} = \frac{\sigma_{\max} l^2}{3Ec}. \tag{4.6}$$

This shows that the allowable elastic deformation grows with the square of the spring length. Consequently, longer springs provide a larger operational range before reaching the yield stress.

To exploit this advantage in limited space, 3D-printed springs can be printed with bends, allowing additional spring length within the same footprint by using a snake-like curve.

4.2.3 Ferris Wheels

The Ferris wheel mechanism is a position measurement device. It functions similarly to a bicycle brake system. A cable runs through a guiding tube and is kept under constant tension by a preloaded spring. Under the assumption of negligible cable stretch, the linear displacement of the cable at one end corresponds directly to the displacement at the opposite end.

One end of the cable is connected to the ATLAS sensor, while the other end is attached to a Ferris wheel assembly. This assembly acts as a pulley system that maintains cable tension using a spring. The spring adds to the effective spring constant of the ATLAS sensor, but it is considered during calibration. The angular position of the pulley is measured using a magnetic absolute encoder (AS5600), allowing the linear displacement of the cable, thus the spring deformation, to be calculated from the measured rotation. The working principle is schematically shown in Figure 4.3.

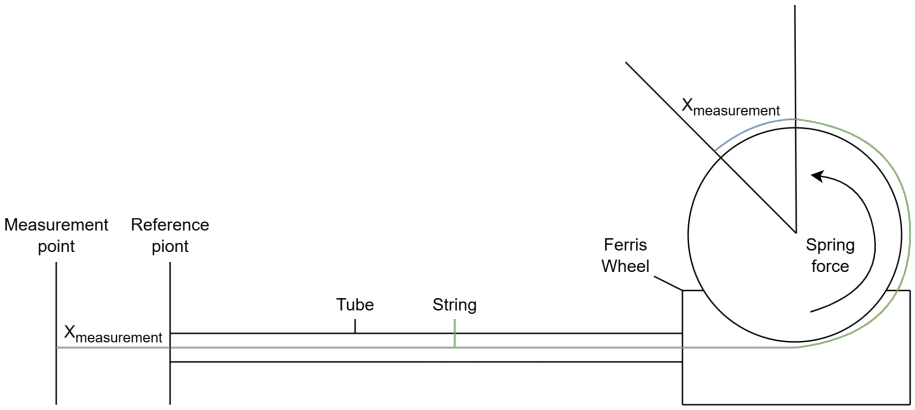


Figure 4.3: Schematic Ferris Wheel Concept

A key advantage of this design is that the Ferris wheel assemblies can be positioned at a safe distance, while the ATLAS sensor itself remains inside the scanner bore. This enables force measurement without introducing MR-unsafe electronic components into the MRI environment. The Ferris wheel mechanism is shown in Figure 4.4.

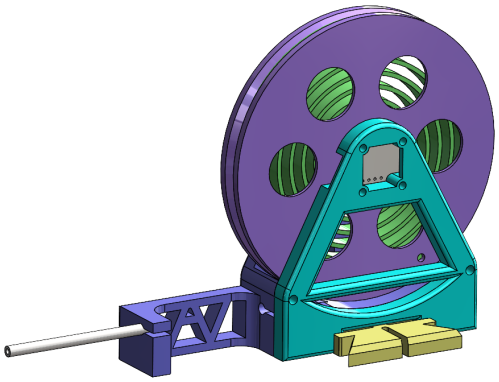


Figure 4.4: Ferris Wheel Mechanism

This Ferris wheel design is stackable and almost entirely 3D-printable. This enables rapid and low-cost fabrication, while also making the design highly accessible for system engineers. The use of 3D printing allows straightforward modification of geometry and integration into different system configurations without requiring specialised manufacturing processes. As a result,

the mechanism can be easily adapted, reproduced, and scaled, which is particularly advantageous during iterative design and experimental validation. The only non-printed components are the magnetic encoder, the rope and the guiding tube.

4.2.4 1-DoF Sensor

The 1-DoF version of the ATLAS sensor is inspired by the torque sensor design presented by He et al. (2024). It consists of two disks connected by a spring. The relative displacement between the disks is measured through an encoder. This displacement is that of the spring and relates to the applied torque.

The prototype of He et al. (2024) is MR-conditional as it employs metallic springs and an off-the-shelf optical encoder. The metallic springs are substituted with 3D-printed springs. This allows for a wide range of spring geometries and materials, which is investigated further using this ATLAS design in Chapter 5.1. The Ferris Wheel replaced the encoder, as previously described in Chapter 4.2.3. To measure the relative angle using the Ferris Wheel, the rope is connected to one disk and the outer guiding tube is connected to the other.

Design

The 1-DoF sensor design consists of three components: a reference base disk, an end-effector disk, and a rotational spring connecting both. The reference disk mounts to the robotic system, represented by the validation framework described in Chapter 4.1. The end-effector disk connects to the end-effector.

The Ferris wheel end can be attached to the reference base and measure the relative displacement of the end-effector disk. The design allows the inner spring to be easily exchanged, facilitating experimentation with different spring materials and geometries.

The final design is shown in Figure 4.5.

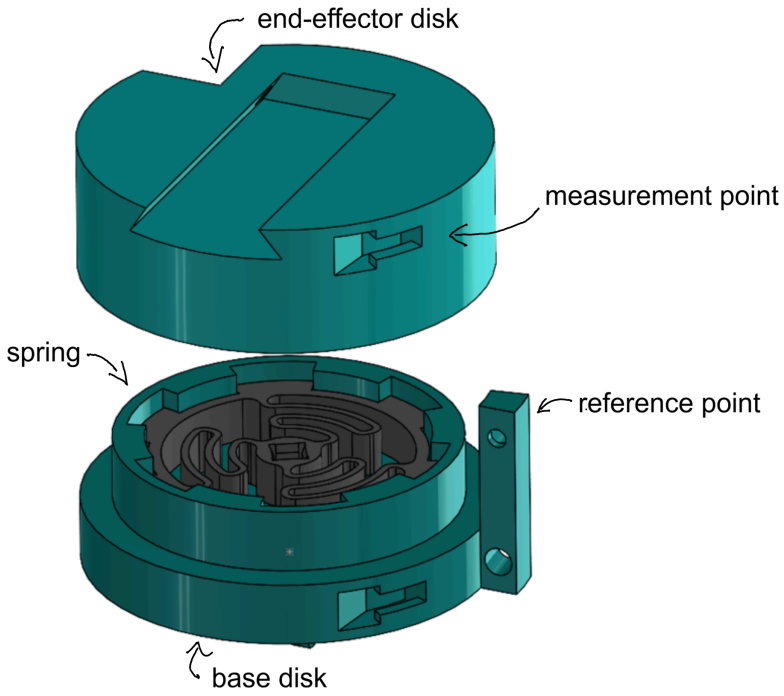


Figure 4.5: 1-DoF ATLAS sensor

Note: This prototype uses an earlier version of the modular interface rather than the current 8-M6 bolt configuration.

4.2.5 3-DoF Sensor

This section describes the design choices behind the 3-DoF ATLAS sensor developed primarily for the MAMRI application. A more detailed description of the complete design is provided in Appendix D.

The 3-DoF sensor design is based on the material study for different spring geometries and materials described in Chapter 5.1. Carbon-fibre-reinforced PLA (PLA-CF) was selected due to its high effective spring constant and low drift.

As discussed in Chapter 4.2.2, longer springs provide a larger operational range before plastic deformation occurs. The effective spring constant can subsequently be tuned by adjusting the spring thickness. A practical description of this tuning procedure is provided in Appendix C.1.1.

Design

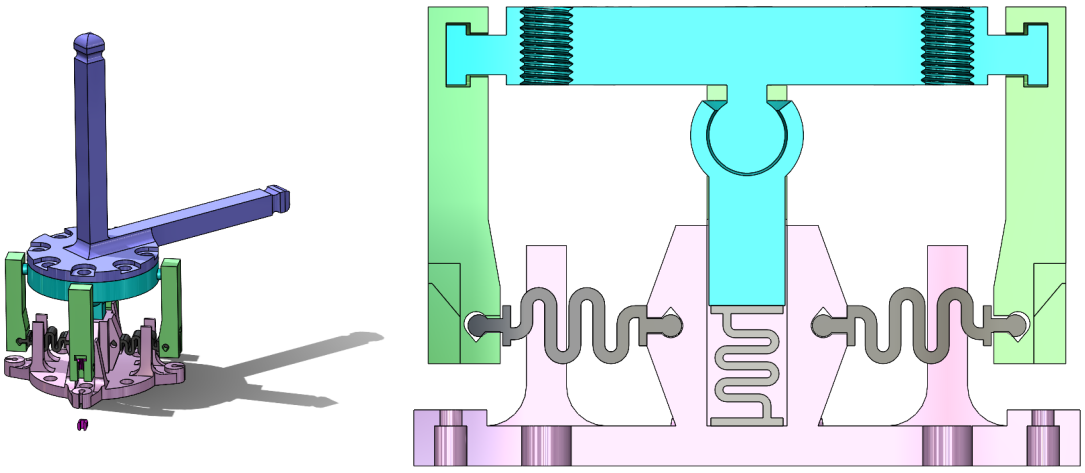
For the 3-DoF ATLAS configuration, a total of four load cells were implemented, including a spring and a Ferris wheel measuring the spring's relative position. This results in an overdetermined system for three degrees of freedom. This geometry was chosen for easy force reconstruction.

In addition, the redundant cell improves measurement accuracy and theoretically enables fault detection. Fault detection indicates a broken system, which is useful for operation, but lies outside the scope of this project and is not yet implemented.

Each cell is connected to a Ferris wheel through a 1 m transmission tube. Although this length is shorter than would be expected in the intended MRI-guided application, it provides a suitable proof-of-principle configuration for evaluating the sensing concept and the mechanical transmission behaviour.

To reduce play, the entire system is mechanically interlocked using a central spring that provides preload. This preload forces any inherent slack in the system to settle into a consistent equilibrium position.

The final 3-DoF ATLAS design is shown in Figure 4.6.



(a) Side view **(b)** Cross section

Figure 4.6: The 3-DoF ATLAS sensor

The design includes the 8-M6 bolt interface, four load cells each measured via a dedicated Ferris wheel, and a central spring that mechanically interlocks the system. This central element reduces joint play and improves overall structural stiffness.

Force Reconstruction

The 3-DoF ATLAS sensor measures force using a coupled load cell configuration. Each load cell consists of a spring element and a displacement measurement of that spring. The displacement is expressed in millimetres from the true zero. The true zero and spring constant values are found through calibration, described in the next section. The K values represent the effective spring constants, where K_{Axial} is in N/mm, and K_{Axial} is in Nm/mm. From a top view of the sensor, the individual load cells are identified according to the cardinal directions (north, east, south, and west).

To reconstruct the force from this measurement, a 3 DoF representation was chosen, as it best captures the relevant interactions at the needle tip (see Chapter 3.3). This representation consists of one axial force and two torque components: pitch and yaw.

When analysing the sensor geometry, an applied axial force results in equal responses from all load cells. In contrast, applied torque produces mirrored results in the load cells, where opposing cells mirror each other. Based on these characteristics, the force components are reconstructed as follows:

1. Compute the average load cell output to estimate the axial force component:

$$x_{\text{avg}} = \frac{x_{\text{north}} + x_{\text{east}} + x_{\text{south}} + x_{\text{west}}}{4} \tag{4.7}$$

$$F_{\text{axial}} = K_{\text{axial}} \cdot x_{\text{avg}} \tag{4.8}$$

2. Subtract the axial contribution from each load cell measurement to isolate the torque-related components.
3. Compute the torque magnitudes for pitch and yaw:

$$\tau_{\text{pitch}} = K_{\text{pitch}} \cdot \frac{|x_{\text{north}} - x_{\text{avg}}| + |x_{\text{south}} - x_{\text{avg}}|}{2} \tag{4.9}$$

$$\tau_{\text{yaw}} = K_{\text{yaw}} \cdot \frac{|x_{\text{east}} - x_{\text{avg}}| + |x_{\text{west}} - x_{\text{avg}}|}{2} \tag{4.10}$$

4. Determine the direction (positive or negative) of both torque components based on which opposing load cell measurement is positive.

Calibration

A calibration procedure is required to compensate for sensor drift and manufacturing deviations. Three key parameters must be determined during calibration:

- True zero
- Linear spring constant
- Torsional spring constant

In an ideal, frictionless system, the sensor would have a unique equilibrium point, making a zero reference straightforward (the position without load). However, in the physical implementation, friction introduces hysteresis into the system, primarily in the Ferris wheel's tubes. Due to hysteresis, the sensor does not return to a single equilibrium point but instead exhibits a range around zero. The midpoint of this range is defined as the true zero, assuming symmetric hysteresis behaviour.

The true zero is determined by identifying the bounds of this equilibrium range. This is achieved by taking two measurements: one after compression and one after extension. The average of these measurements is defined as the true zero.

The spring constants are calibrated to account for drift in the effective spring constants. These constants are determined by applying a known load to the system and measuring the resulting

displacement. Rather than relying on a single measurement, the result is obtained as the average of 10 samples to reduce noise. To further mitigate hysteresis effects, measurements should ideally be taken for both increasing and decreasing loads. Using the known applied load, the calculated average displacement, and the previously determined true zero, the spring constant is computed.

A dedicated calibration end-effector was developed to ensure consistent and repeatable force application. For linear calibration, the end-effector includes a mounting point for a 1 kg mass, 9.81 N axial force at the centre of the sensor. For torsional calibration, it features two 100 mm lever arms (yaw and pitch), allowing a 250 g mass to be suspended, generating 0.245 Nm of torque.

Although the effective torsional spring constants for yaw and pitch may differ slightly due to manufacturing inconsistencies, this difference is considered negligible. To simplify the calibration procedure, a single torsional spring constant is assumed for both degrees of freedom.

Demo Setup with Indication

A demonstration setup was developed to demonstrate the sensor's responsiveness and accuracy. The setup consists of the 3 DoF ATLAS sensor (Chapter 4.2.5, which is read out through four Ferris Wheels (Chapter 4.2.3. Since all encoders share the same I2C address, an I2C multiplexer is required to enable communication with each sensor.

The I2C multiplexer communicates with an ESP32-C5 microcontroller. This microcontroller was chosen for its support for 5 GHz Wi-Fi, which operates in a different frequency band than most other devices in the laboratory (typically 2.4 GHz). This reduces network congestion and ensures more reliable communication.

A schematic overview of the electrical circuit is illustrated in Figure 4.7.

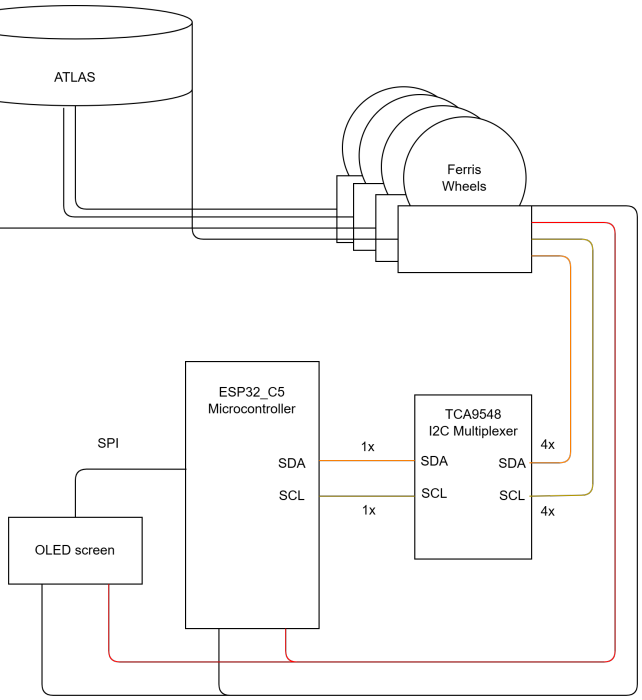


Figure 4.7: Electrical circuit of the demo setup

To provide clear feedback and interaction, a web application was developed as an indication method. The web interface displays:

- Real-time measured sensor values
- Current positions of the sensors
- Measurement history visualised through graphs

All visualisations are rendered client-side to ensure a quick 5 Hz update cycle.

In addition to data visualisation, the web application includes an interactive game for open days and technical events at the University of Twente. It is designed to be plug-and-play and serves as an engaging way to attract visitors and introduce them to the project. For common demo operation, a manual is presented in Appendix A

4.3 AEOLUS

Airflow Encoded Output for Load-Utility Sensing

4.3.1 Method

The AEOLUS sensor extends the work of Rie (2024), which investigated force estimation by compressing a pneumatic hose and measuring the resulting pressure change. While this principle establishes a clear relationship between compression force and air pressure response, experimental evaluation showed that pressure differences saturated quickly once the hose was fully constricted. Air pressure is influenced by airflow and container volume. As a result, accurate force estimation would require highly sensitive pressure sensors and short pneumatic paths, both of which are impractical in the present application.

To overcome these limitations, the AEOLUS method shifts from pressure-based sensing to airflow-based sensing. This should reduce the amount of pneumatic path-length-based challenges since volume is no longer an issue. Instead of measuring a pressure difference, the applied force is inferred from the steady-state airflow.

External loading compresses the sensor, which modulates a controlled leakage path. Increased compression increases airflow, establishing a relationship between the applied force and the airflow rate. The pneumatic chamber within the sensor acts as a self-generated spring through its internal pressure, eliminating the need for additional springs.

4.3.2 Flow Sensors

Airflow is measured using a turbine-based sensing principle. The air stream drives a small rotor that is mechanically coupled to a DC motor operating as a generator. As airflow increases, the rotor's rotational speed increases, raising the output voltage. The measured voltage, therefore, indicates the airflow rate.

The flow sensor assembly consists of an enclosed airflow chamber integrated between two rigid plates. An O-ring is compressed between the plates to form an airtight seal, ensuring that all airflow is routed through the air chamber. The DC motor is mounted at the rear of the chamber, with its shaft directly coupled to the airflow-driven rotor. A cross-section of the flow sensor is shown in Figure 4.8.

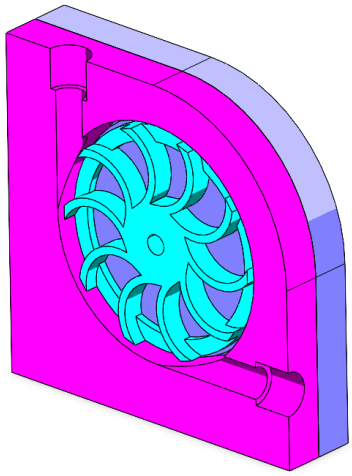


Figure 4.8: Flow sensor cross-section

4.3.3 1 DoF

The 1 DoF implementation acts as a proof of concept and resembles the simplest realisation of the AEOLUS sensing principle. This section describes the functionality and the role of this proof-of-concept within the project; a more detailed description is given in Appendix E. As stated in the method description, Section 4.3.1, the goal is to couple the output airflow with the applied force.

Applied force will alter the state of the air chamber within the sensor. The air chamber is designed with a controlled-leakage path that regulates airflow as the chamber deforms. A cross-sectional view of the 1 DoF air chamber is shown in Figure 4.9. The primary airflow channel runs from left to right through the structure.

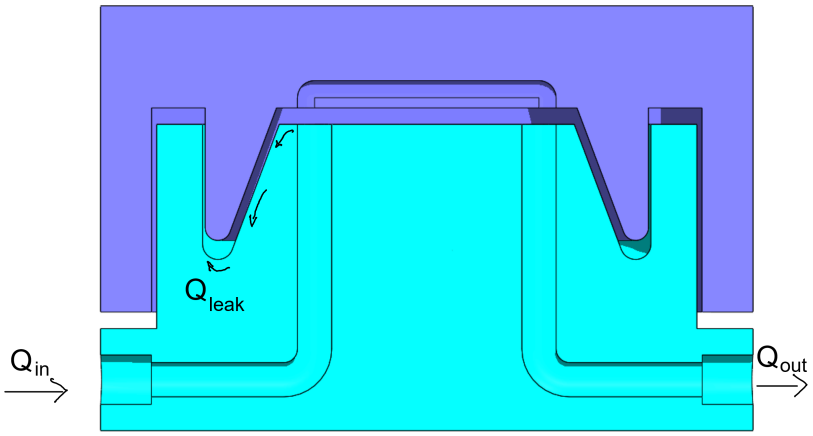


Figure 4.9: Cross-sectional view of the 1 DoF airchamber

When the internal pressure of the air chamber exceeds the ambient pressure (i.e., greater than 1 bar), a net force acts on the roof of the chamber. This causes the chamber to expand until the mechanical limit of 8 mm is reached. As the chamber expands, the separation between these layers increases, enlarging the leakage opening. This creates a passive coupling between mechanical displacement and airflow.

Given Newton's third law, the applied force must be balanced by the force exerted by the pressurised air inside the chamber:

$$F_{\text{applied}} = F_{\text{air}} \tag{4.11}$$

The force generated by the air pressure is given by

$$F_{\text{air}} = (P_{\text{chamber}} - P_{\text{ambient}}) \times A \tag{4.12}$$

where A denotes the effective area of the sensor, approximately $1200\,\text{mm}^2$. Alternatively:

$$\Delta P = P_{\text{chamber}} - P_{\text{ambient}} = \frac{F_{\text{applied}}}{A} \tag{4.13}$$

To determine the resulting airflow, the leakage through the chamber must be considered. The output airflow equals the supplied airflow minus the leakage flow:

$$Q_{\text{out}} = Q_{\text{in}} - Q_{\text{leak}} \tag{4.14}$$

The leakage path within the chamber can be approximated as flow through a thin rectangular gap. The corresponding volumetric flow rate is

$$Q_{\text{leak}} = \frac{wh^3}{12\mu L}\Delta P \tag{4.15}$$

where w, h, and L describe the geometric dimensions of the gap, μ is the dynamic viscosity of air, and ΔP is the pressure difference between the chamber and the ambient environment.

Substituting the pressure relation results in

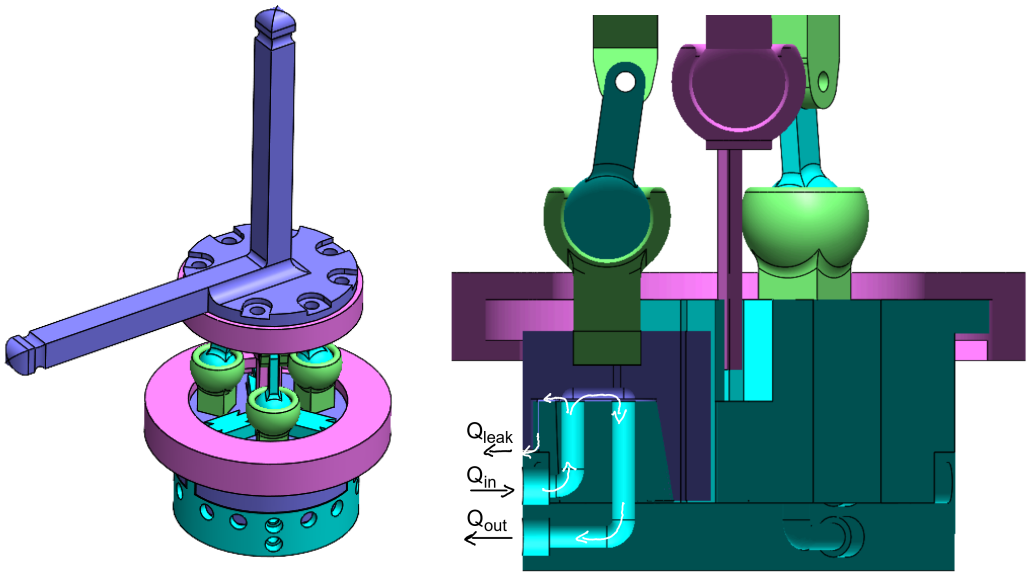
$$Q_{\text{out}} = Q_{\text{in}} - \frac{wh^3}{12\mu L}\frac{F_{\text{applied}}}{A} \tag{4.16}$$

This relationship was linearised, as h does not exceed 8 mm due to mechanical constraints. In reality, the relationship between output flow and applied force is S-shaped. At low forces, a threshold must be overcome to counteract static friction in the chamber. At higher forces, h approaches zero, indicating that the chamber is fully compressed, and further increases in force do not result in additional output flow.

4.3.4 3 DoF

The promising behaviour of the 1 DoF proof-of-concept design motivated the development of a 3 DoF version. This design aims to measure forces in three directions using three pneumatic chambers. Each chamber provides independent airflow measurements, allowing the system to reconstruct three-dimensional force through coupled chamber responses (see Appendix F for a detailed description of the design).

The operating principle remains identical to that of the 1 DoF design. However, the single air chamber is divided into three separate compartments, each with its own inlet and outlet airflow path. A model of the design is shown in Figure 4.10.



(a) Side View **(b)** Cross Section

Figure 4.10: The 3 DoF AEOLUS

Despite the conceptual similarity to the 1 DoF design, the 3 DoF implementation did not perform as expected. As per requirement TR03.02, the system must fit within the MAMRI circular footprint. To fit three chambers within that footprint, the chamber area had to be significantly reduced. The effective chamber area decreased from approximately 1200 mm^2 in the 1 DoF design to 155 mm^2 per chamber.

This reduction in chamber area directly affects the required chamber pressure. The force generated by the pneumatic chamber is given by

$$F = (P_{chamber} - P_{ambient}) \times A \tag{4.17}$$

To generate an output force of 15 N, the required chamber pressure becomes

$$P_{chamber} = \frac{F}{A} + P_{ambient} = \frac{15}{115 * 10^{-6}} + 1 = 230434\,\text{Pa} = 2.3\,\text{Bar} \tag{4.18}$$

Although supplying air at 2.3 bar absolute pressure is not inherently problematic, the corresponding airflow demand becomes prohibitively large. Further investigations show that the sensor consumes 340 L/min of air at atmospheric pressure, described in Chapter 5.7.

The effective volumetric flow inside the chamber can be estimated using the pressure ratio relation

$$Q_{chamber} = Q_{out} * \frac{P_{ambient}}{P_{chamber}} \tag{4.19}$$

$$340 * \frac{1}{2.3} = 147.82\,\text{L/min} \tag{4.20}$$

This flow rate is extremely high and would require a pressure regulator capable of delivering at least 150 L/min at 2.3 bar. Such requirements are unrealistic for the intended application, making the current 3 DoF implementation impractical.

5 Tests

5.1 ATLAS Spring Materials

The goal of this test is to determine the most suitable material for the springs within the ATLAS sensor. The springs should be robust and predictable. Evaluation is based on linear behaviour, effective spring constant, and drift. Linear behaviour is necessary for predictable behaviour. A high spring constant requires smaller springs for the same forces. Low sensor drift will require fewer calibration cycles.

5.1.1 Setup

The 1 DoF ATLAS model was designed to iterate different spring materials and geometries, Chapter 4.2.4. It was mounted to the validation framework described in Chapter 4.1.

The resulting setup has a single rotational degree of freedom, a Ferris wheel to measure the relative angular displacement, and a 100 mm lever from which weight can be suspended to apply a controlled torque. The experimental setup is shown in Figure 5.1.

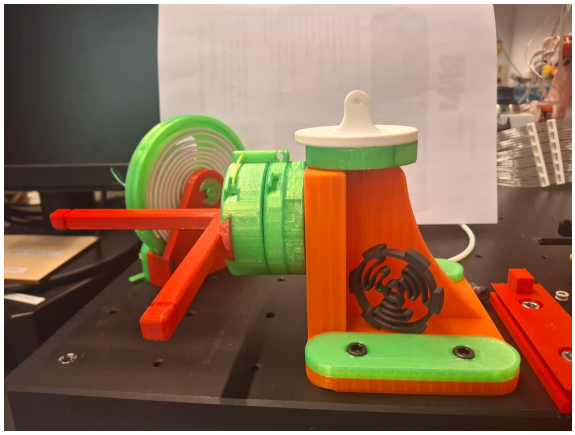


Figure 5.1: Test Setup Spring Materials

In Section 4.2.2, it was shown that spring geometry affects spring behaviour, and that longer springs generally provide more favourable characteristics. Based on these findings, the geometry shown in Figure 5.2 was selected for this test.

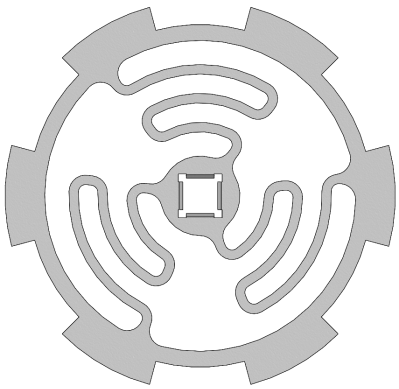


Figure 5.2: Spring Geometry

The spring geometry is printed using three different spring materials. The selected materials are common in 3D-printed springs:

- PETG
- PCTG
- CF-PLA

5.1.2 Method

To apply controlled torque, a weight is suspended from a rotating lever arm. This rotation is significant and will alter the torque generated. This situation is schematically shown in Figure 5.3.

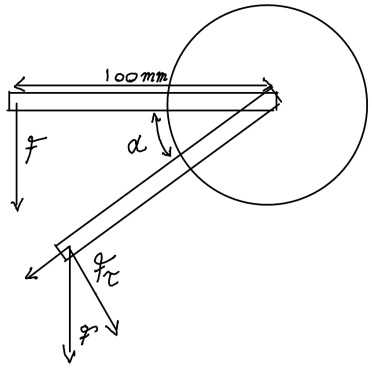


Figure 5.3: Torque generation at an angle

The resulting torque can be calculated given the measured angle α:

$$\tau = F_{\text{downwards}} \times cos(\alpha) \times 0.1 \tag{5.1}$$

As mentioned before, springs are evaluated based on their drift and spring constant. They are measured separately.

Drift

A 0.5 kg weight is suspended from the end of the lever arm. The load is applied for at least three days. Each day, the sensor measures the angular position, and its value is recorded.

Stiffness

Weights up to 1 kg are suspended from the lever arm in increments of 20 grams. At each increment, the sensor measures the angular position, and its value is recorded.

5.1.3 Results

Drift results are given as the average drift per day. The found effective spring constants and average drift per day are shown in Table 5.1.

All materials showed linear behaviours. This is explained in further detail in Appendix C.2.2.

Table 5.1: Measured drift rates and spring constants of the tested spring materials

	Drift	Spring Constant
PLA-CF	0.20 deg/day	0.041 Nm/deg
PCTG	0.43 deg/day	0.014 Nm/deg
PETG	1.10 deg/day	0.016 Nm/deg

5.1.4 Conclusion

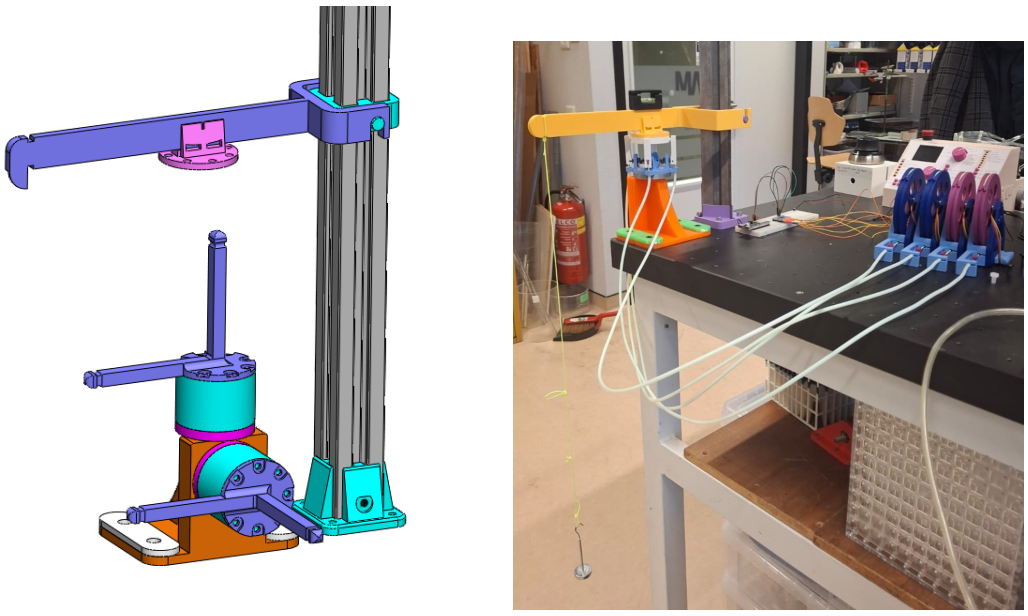
PLA-CF was selected as the most suitable spring material. It has the highest stiffness, allowing for a smaller overall sensor footprint. It also has a lower drift, requiring fewer calibration cycles.

5.2 ATLAS 3 DoF Functionality Test

The objective of this test is to characterise the performance of the 3-DoF ATLAS sensor. In accordance with the requirements defined in Chapter 3.6.2, this includes the sensor's accuracy and resolution over an operating range of up to 150% (22.5 N in axial force and 0.45 Nm in torque).

5.2.1 Setup

The validation framework was designed to apply controlled forces on the sensor in Chapter 4.1. It uses calibrated weights to generate the force, which is transmitted through levers into the correct force orientation. The 3 DoF ATLAS sensor is placed within this setup for examination. The full setup is shown in Figure 5.4.



(a) Design **(b)** Real Setup

Figure 5.4: ATLAS Validation Framework

5.2.2 Method

The sensor's accuracy and resolution are characterised by determining its effective spring constants in axial force and torque. Known loads are applied with increments of 20 grams, allowing the corresponding deflections to be measured. From these measurements, the effective spring constants are estimated, forming a linear model of the sensor response. Deviations between the measured response and this linear model are used to quantify the sensor accuracy.

Knowing the Ferris wheel resolution and the effective spring constant, a force measurement resolution was calculated.

Axial Force

In Chapter 4.2.5, it is explained that the average measurement of the four load cells equals the axial force. Since the 3 DoF ATLAS sensor is a coupled setup, no additional torques must be generated when applying axial force. This is achieved using an end-effector attachment

mounted on top of the sensor that aligns the lever with the sensor axis, Figure 5.4b. Force is now focused at the centre of the sensor, minimising the generation of additional torques.

The relation between the weights and the applied force is found in Chapter 4.1.

$$F_{\text{axial}} = (m_{\text{weights}} \times \frac{l_{\text{total}}}{l_{\text{sensor}}} + m_{\text{arm}}) \times g \tag{5.2}$$

The length of this lever to the sensor centre is $l_{\text{sensor}} = 130\,\text{mm}$ and $l_{\text{total}} = 300\,\text{mm}$. The lever weight is 84 g. This gives the following relation between force and weight:

$$F_{\text{axial}} = (m_{\text{weights}} \times \frac{0.3}{0.12} + 0.084) \times 9.81 \tag{5.3}$$

Weights will range up to 1 kg, applying up to 25 N of force, with increments of 20 grams.

Torque

For the torque experiment, a different end-effector attachment is used that introduces a 100 mm lever arm on top of the sensor. Weights are suspended from the end of this arm, generating a torque about the sensor axis. The force-weight relation was also found in Chapter 4.1.

$$\tau_{\text{yaw/pitch}} = m_{\text{weights}} \times l_{\text{lever}} \times g \tag{5.4}$$

With the known lever distance of $l_{\text{lever}} = 100\,\text{mm}$.

$$\tau_{\text{yaw/pitch}} = m_{\text{weights}} \times 0.1 \times 9.81 \tag{5.5}$$

As mentioned before, the configuration introduces a small horizontal force when the system rotates. However, the sensor displacement is limited to a maximum travel of 5 mm, which results in a maximum rotation of 9 degrees. This rotation is small enough to neglect the horizontal force component.

5.2.3 Results

Figure 5.5 shows the averaged measurement together with the fitted linear model. This model was fitted using a least-squares regression approach. The found effective spring constant is 20.49 N/mm.

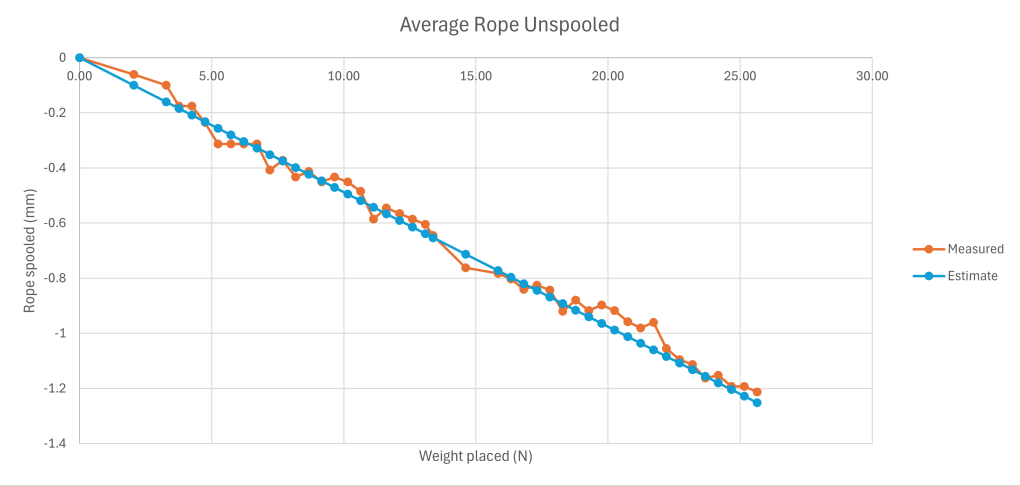
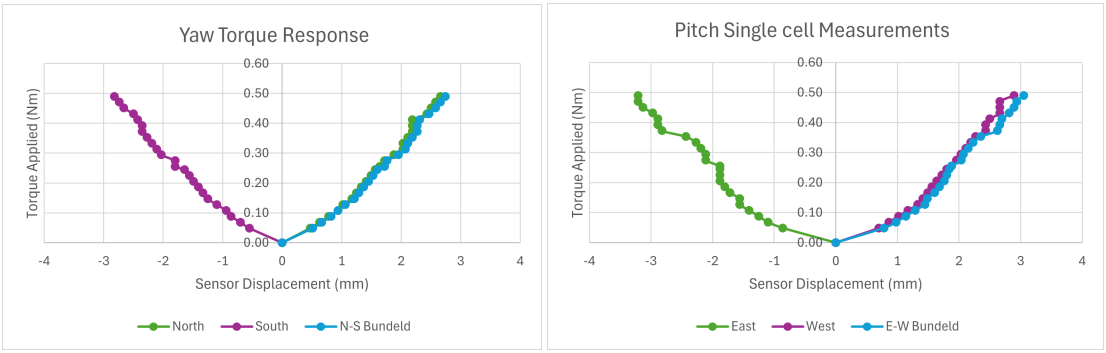


Figure 5.5: Average displacement of the load cells compared with the linear model

Figure 5.6 shows the torque response of the sensor. As explained in Chapter 4.2.5, the absolute average is used to gain accuracy; this graph is also shown in the figure. The found effective spring constant for both torques is 0.19 Nm/mm.



(a) Yaw **(b)** Pitch

Figure 5.6: Measured torque responses of the sensor

For all measurements, it can be seen that before entering the linear domain, there is a slight curve hinting at hysteresis. Both axial force and torque measurements meet the 150% maximum force requirement and will measure to that mark reliably.

Accuracy

Accuracy within the report is defined as two standard deviations, assuming a Gaussian distribution. This means that 95% of the measurements will fall within the accuracy range. The found accuracies are:

- Axial Force: ±1.1 N
- Torque Yaw: ±0.103 Nm
- Torque Pitch: ±0.124 Nm

Resolution

Resolution is limited by the ADC within the AS5600 encoders. This ADC has 12 bits, thus 4096 steps. The Ferris wheel has a diameter of 102 mm. The resolution in millimetres of rope is:

$$\frac{102\pi}{4096} = 0.078\,\text{mm} \tag{5.6}$$

Given the known spring constants and amount of load cells used per measurement (4 for axial force and 2 for torque), this gives the following force resolutions:

- Axial Force: 0.400 N
- Torque: 0.007 Nm

5.2.4 Conclusion

The found resolutions do meet the requirements. The found accuracies do not meet the requirements. However, the achieved performance is still promising for a prototype system. It may also be questioned whether these target accuracies are strictly necessary, as the absolute force value is often less important than the ability to detect changes in force. This topic is discussed further in Chapter 6.1

The results suggest that hysteresis effects significantly influence the measurement accuracy. This behaviour is investigated further in a separate test.

5.3 ATLAS 3 DoF Hysteresis Tests

Initial testing on the 3 DoF ATLAS sensor showed signs of hysteresis. As described in Chapter 4.2.5, the sensor is mechanically interlocked and therefore has a single natural steady-state position. However, the Ferris wheel system experiences hysteresis, likely due to friction between the rope and guiding tubes. As a result, the measured steady-state position depends on whether the sensor approaches equilibrium from compression or extension.

This behaviour significantly affects the sensor's accuracy. The objective of this test is to characterise the behaviour and to explore the concept of hysteresis compensation.

5.3.1 Setup

The experimental setup consists of the 3 DoF ATLAS sensor mounted in the validation framework. This is a similar setup as shown in Figure 5.4. To apply force to the system, the calibration end-effector is used, described in Chapter 4.2.5. The tube length between the Ferris wheels and the sensor is 1 meter.

5.3.2 Method

Hysteresis is evaluated by analysing the steady-state position. The sensor is first calibrated using the procedure described in Chapter 4.2.5, which determines the true zero position. Deviations from this true zero indicate the hysteresis.

These deviations were measured after compression and extension in alternating order. The sensor is compressed by placing a 1 kg weight on the calibration end-effector. After removing the load, the deviation from true zero is documented. Secondly, the sensor is extended by lifting the full setup with 1 kg placed at the base. The total assembly weight equals 1.5 kg. After release, the deviation from true zero is documented. This cycle was repeated 15 times.

5.3.3 Results

Figure 5.7 shows the hysteresis response for each Ferris wheel. During testing, it was observed that the speed at which the sensor returns to steady state influences the magnitude of the error. The average hysteresis deviation was 0.25 mm.

In addition, hysteresis was found to depend on the individual Ferris wheels themselves. The hysteresis behaviour is not consistent across all Ferris wheels. Small inconsistencies between sensors resulted in different behaviours.

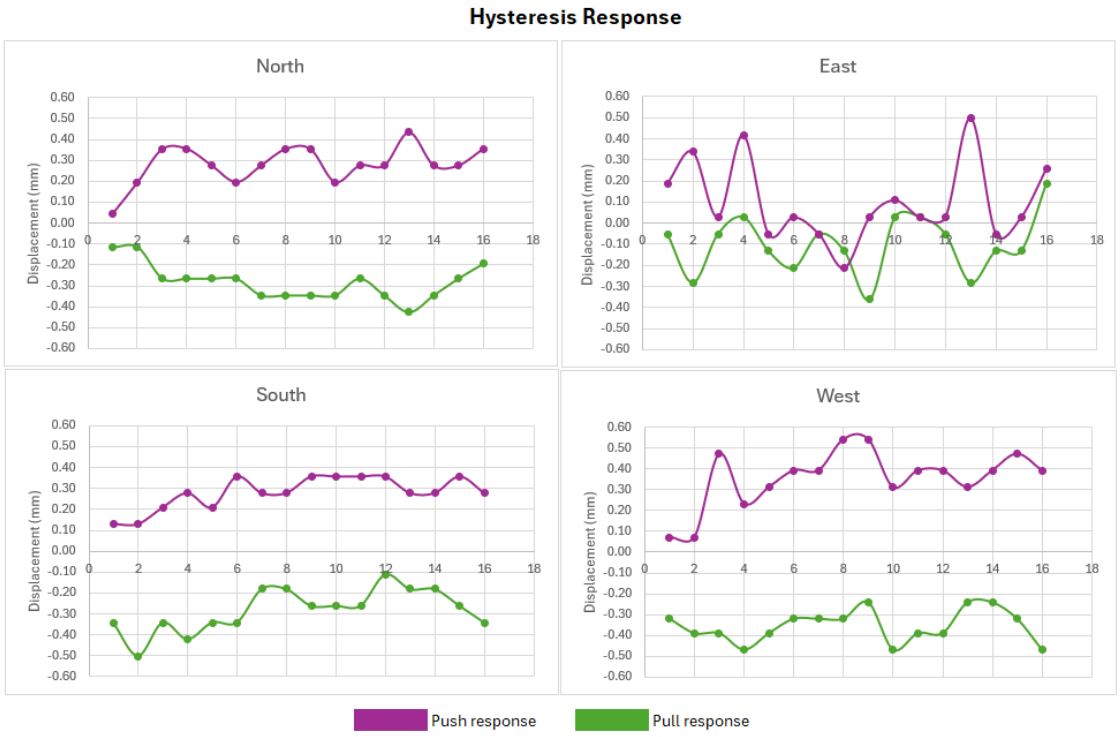


Figure 5.7: ATLAS Hysteresis Response over different iterations

5.3.4 Conclusion

Inconsistencies between sensors gave variable hysteresis behaviours. Furthermore, the magnitude of the hysteresis is not consistent and depends on multiple variables. The average hysteresis deviation was 0.25 mm. Future work should focus on reducing hysteresis at the mechanical level to improve overall sensor performance. Hysteresis compensation will be difficult due to its unpredictable behaviour.

5.4 ATLAS 3 DoF Drift Test

The goal of this test is to investigate the long-term behaviour of the ATLAS sensor. As shown in Chapter 5.1, 3D-printed spring materials exhibit drift over time. PLA-CF was selected due to its relatively low drift behaviour compared to the other materials. This experiment aims to evaluate the drift of the complete 3 DoF ATLAS system under a constant load over an extended period.

5.4.1 Setup

The sensor was mounted inside the validation framework described in Chapter 4.1, using the same configuration as shown in Figure 5.4. Unlike previous experiments, the lever-arm construction was replaced by a centred 1 kg mass placed directly on top of the sensor. This configuration applies a constant axial load to the system. The setup was left undisturbed for seven days.

5.4.2 Method

The setup described above was monitored over all seven days. At regular intervals, the sensor state was recorded and compared to the initial calibrated state. Drift was evaluated based on three quantities:

- Relative rope displacement measured by the Ferris wheel mechanisms,
- Measured axial force output,
- Calculated spring constant.

5.4.3 Results

The measured average drift rates are shown in Table 5.2.

Table 5.2: Average drift rates of the 3-DoF ATLAS sensor.

Drift Quantity	Average Drift Rate
Rope displacement drift	0.008 mm/day
Force drift	0.12 N/day
Spring constant drift	0.42 $\mathrm{N\,mm^{-1}\,day^{-1}}$

5.4.4 Conclusion

The measured drift rates are relatively low compared to the operating range of the sensor. These results indicate that the PLA-CF spring configuration provides sufficiently stable behaviour.

The observed drift indicates the required calibration frequency. The acceptable interval between calibration cycles depends on the accuracy requirements of the intended application and the drift values presented in Table 5.2.

5.5 ATLAS 3 DoF Integration Test

Requirement SR01.01 states that the sensor must be modular to enable integration into different systems. The ATLAS method is promising and has resulted in a 3 DoF design for the MAMRI robot, designed in Chapter 4.2.5.

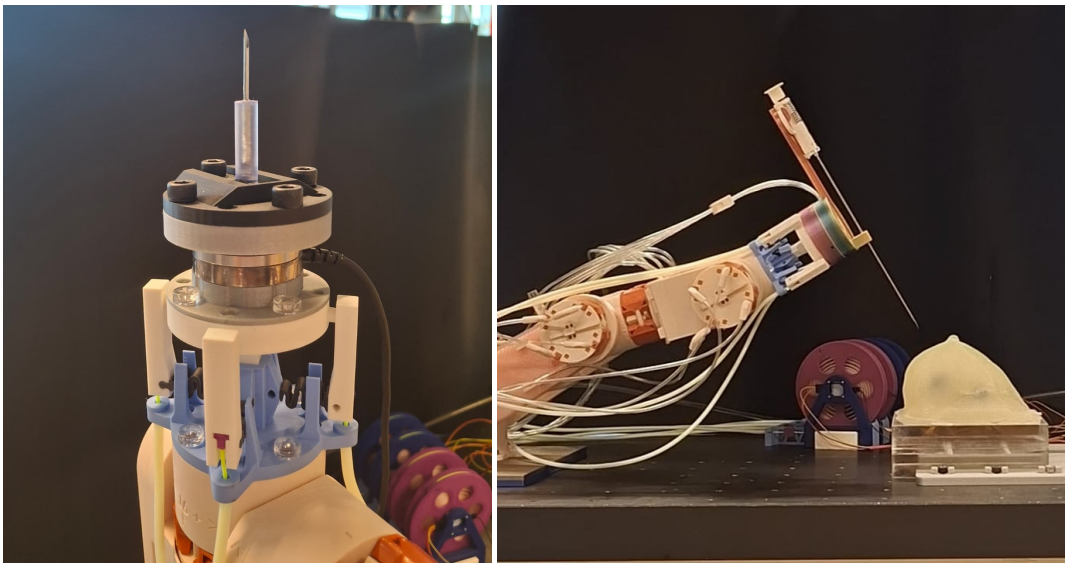
This test evaluates the integration of the ATLAS sensor within the MAMRI robotic arm and assesses its behaviour and measurement accuracy.

5.5.1 Setup

The ATLAS sensor is mounted between the MAMRI robotic arm and its end-effector. The original test configuration has the needle aligned with the sensor's force axis. However, this configuration differs from the actual implementation on the MAMRI arm, where the needle is mounted perpendicular to the arm and actuated via a linear motor. A phantom breast is used as a reference for punctuation.

Both configurations are tested:

- **Axial (straight needle) load case:**, Figure 5.8a. The focus lies on the axial force, as this is the most dominant force. An additional 6 DoF force sensor (ATI Mini40) is placed in series with the ATLAS sensor to measure the applied axial force. Since both sensors experience the same load, the difference between their measurements provides an estimate of the absolute error. (Automation, n.d.)
- **Perpendicular needle load case:**, Figure 5.8b. The focus lies on the torque; punctuation will twist the system, applying a torque as the most dominant force. No additional force sensor is used, as this would increase the lever length and applied torque. Instead, this test focuses on detecting relative changes in force.



(a) Straight needle load case **(b)** Perpendicular needle load case

Figure 5.8: Test configurations for the ATLAS sensor

5.5.2 Method

Before the test, both sensors are calibrated. The duration of the test is at least one minute and contains at least one punctuation in a phantom breast.

Through software, both the ATLAS and ATI Mini40 force sensors were recorded and stored as CSV files. A video recording started simultaneously with the software. All measurements and

recordings are timestamped, allowing visual events to be correlated with both measured forces. For the perpendicular needle configuration, the ATI sensor is removed.

5.5.3 Results

Markers in the graphs indicate the timestamps at which specific events occurred during the experiments.

Figure 5.9 shows the axial configuration results. The sensor accuracy is 1.5 N at two standard deviations. The 3 DoF ATLAS sensor closely follows the ATI measurements, demonstrating good agreement with the applied force. Hysteresis is still in play.

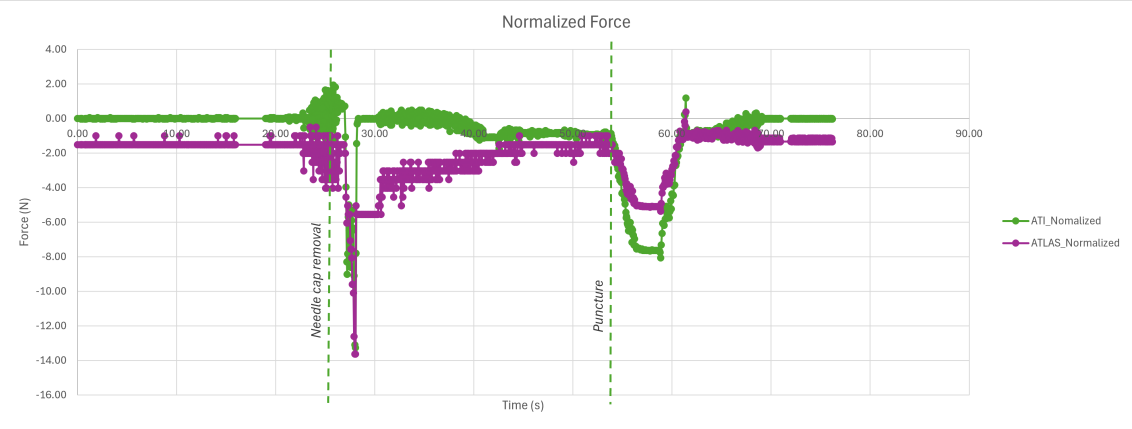


Figure 5.9: Straight Needle Load-case Results

Figure 5.10 shows the perpendicular configuration results. The sensor output clearly reflects the different interaction phases of the robotic arm.

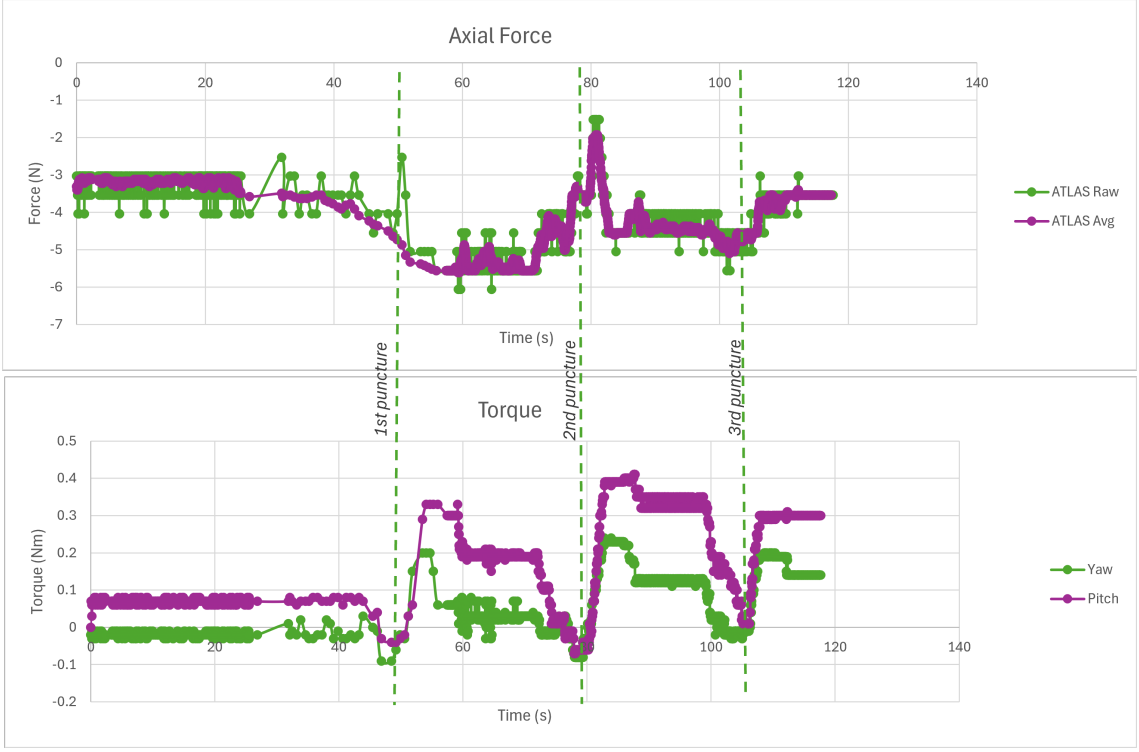


Figure 5.10: Perpendicular Needle Load-case Results

5.5.4 Conclusion

The test demonstrates a good integration of the ATLAS force sensor with the MAMRI robotic arm. In the axial configuration, the sensor achieves a reasonable level of accuracy, although hysteresis effects remain visible.

In the perpendicular configuration, the sensor successfully captures relative force changes. This indicates that the sensor can provide meaningful feedback about the needle's interaction with its environment, even without a direct visual.

5.6 AEOLUS 1 DoF Sensor

The 1 DoF AEOLUS setup, introduced in Chapter 4.3.3, was experimentally evaluated to assess its performance. The expected behaviour is a linear relationship between the applied force and the resulting output voltage. In addition to verifying this relationship, the experiments aimed to determine the most suitable electrical configuration for the system.

The standard configuration is an open-circuit condition, in which the voltage difference across the terminals of the DC motor in the flow sensor is measured directly. As an alternative, a short-circuit configuration was considered, effectively increasing electrical damping in the system. This configuration is expected to produce lower voltage amplitudes, reduce oscillations and improve settling time.

The response of the setup under both configurations is investigated and compared in this test.

5.6.1 Setup

The 1 DoF AEOLUS sensor described in Section 4.3.3 was tested in combination with the flow sensor presented in Section 4.3.2. The output voltage generated by the DC motor within the flow sensor was measured across the motor terminals.

Measurements were performed under two electrical configurations: open-circuit and short-circuit. In the latter, a diode was connected across the motor terminals, introducing electrical damping when the current increases.

5.6.2 Method

A controlled axial force was applied to the 1 DoF AEOLUS sensor by placing weights on top of the force sensor in increments of 40 grams. At each increment, the system was given time to reach a steady-state voltage, after which the output voltage was recorded. This was done in both open- and short-circuit configurations.

5.6.3 Results

The results for the open-circuit configuration are presented in Figure 5.11, while the results for the short-circuit configuration are shown in Figure 5.12. Measurements are reported starting from an applied force of 10 N, as this was the threshold at which the externally applied force exceeded the opposing force generated by the air pressure within the chamber.

The open-circuit configuration required around 30 seconds per measurement for the flow sensor to reach a steady state. The closed-circuit configuration required significantly less settling time, approximately 5 seconds per measurement.

A linear trendline is included in each figure to assess the linearity of the results.

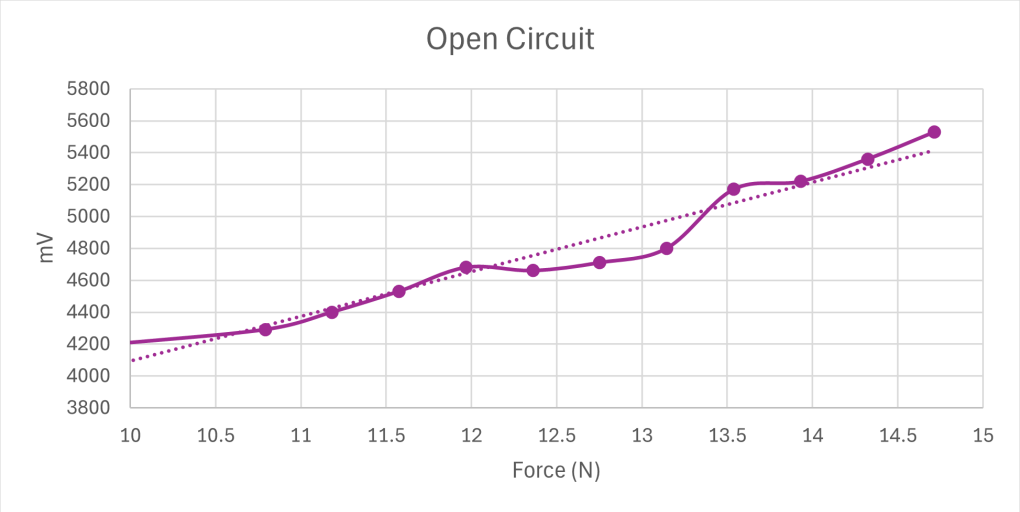


Figure 5.11: Open Circuit Results: Output voltage over Applied Force

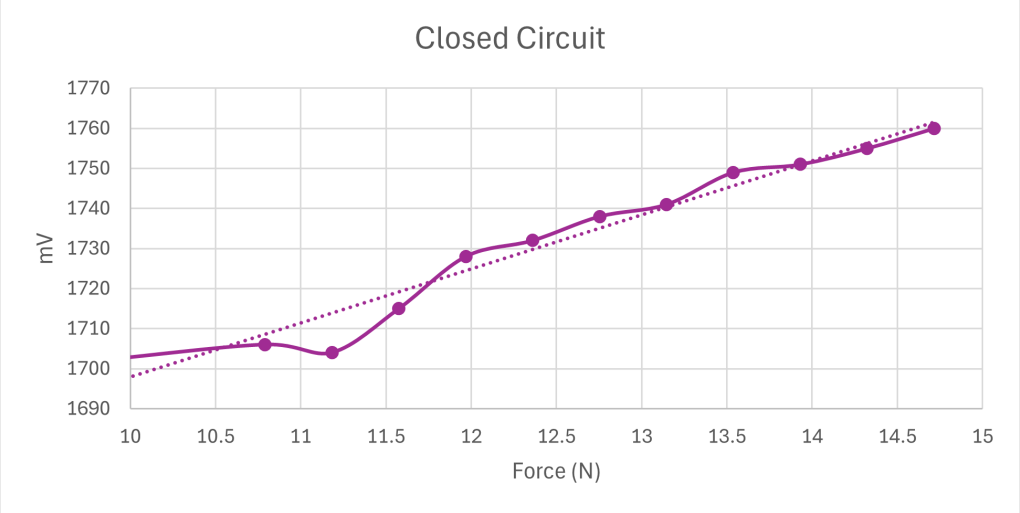


Figure 5.12: Closed Circuit Results: Output voltage over Applied Force

5.6.4 Conclusion

The first conclusion is that the linearization of the relationship between the applied force and the measured output voltage was correct. In both configurations, the system shows linear behaviour.

The second conclusion is that a short-circuited configuration is preferred as it demonstrates reduced settling time and fewer oscillations compared to the open-circuit configuration. Although the measured output voltages in the closed-circuit case were lower, this is not a limitation for typical onboard ADCs.

5.7 AEOLUS 3 DoF Sensor

The promising behaviour observed in the 1 DoF sensor does not directly translate to the 3 DoF design. Due to the reduced air chamber volume, the system experiences significant pressure losses. This is shown analytically in Chapter 4.3. The pressure loss is too significant to take meaningful measurements on the system in its current configuration. The output airflow cannot overcome the internal friction within the flow sensors.

This experiment aims to find the actual airflow used by the system.

5.7.1 Setup

An air compressor with a known tank volume is used to estimate the airflow through the sensor. The sensor's input is directly mounted to the compressor, while its output is connected to the flow sensors. Although the flow sensors do not produce a measurable voltage (as they do not rotate under these conditions), they simulate a realistic output resistance.

5.7.2 Method

The air compressor tank is pressurised to 6 bar. Upon opening the valve, air flows through the sensor, causing the tank pressure to decrease. During the measurement, the compressor is switched off to prevent refilling. The time required for the pressure to drop from 6 bar to 5 bar is recorded and used to estimate the airflow.

The airflow estimation assumes ideal gas behaviour and constant temperature. Starting from the ideal gas law, the molar flow rate can be related to the pressure change as:

$$\dot{n} = \frac{V_{\text{tank}}}{RT} \cdot \dot{p} \tag{5.7}$$

Expressing this as a volumetric flow rate at ambient conditions yields:

$$\dot{V}_{\text{air}} = \frac{V_{\text{tank}}}{P_{\text{amb}}} \cdot \dot{p} \tag{5.8}$$

Using a finite difference approximation, the flow rate is computed as:

$$\dot{V}_{\text{air}} = \frac{V_{\text{tank}}}{P_{\text{amb}}} \cdot \frac{\Delta P_{\text{tank}}}{\Delta t} \tag{5.9}$$

P_{amb} is the ambient pressure, measured as 99,900 Pa during testing. V_{tank} is the known tank volume of 50 L.

This method relates observed pressure decay time to the resulting normalised airflow. Measurements are performed for two mechanical states of the sensor: fully compressed (with a 1 kg applied load) and uncompressed (no load). Both states are evaluated at chamber pressures of 2 and 3 bar, corresponding to the intended operating pressure of 2.3 bar found in Chapter 4.3.4.

5.7.3 Results

Table 5.3: Measured airflow under varying pressure and load conditions

Pressure (kPa)	Weight on system	Time (s) (6→5 bar)	$\dot{V}$ (m^3/s)	$\dot{V}$ (L/min)
3	0	8.85	0.005655	339.32
3	1000	13.19	0.003795	227.67
2	0	12.22	0.004096	245.74
2	1000	15.55	0.003219	193.12

5.7.4 Conclusion

The measured air consumption is significantly high for the application in each load case in Table 5.3. This indicates that the current setup exhibits too much air leakage.

Although each condition was evaluated only once, limiting the accuracy of the absolute values, the consistently high airflow across all measurements is enough to conclude insufficient behaviour.

Further optimisation of the sensor design is required to reduce air consumption. A detailed investigation of this aspect falls outside the scope of the study. The focus was placed on the ATLAS sensor due to its better scalability.

6 Discussion

The discussion reflects on the results presented in the main body of this report and places them into a broader technical and application-oriented context. The focus lies on three aspects: the comparison between the results and the predefined system requirements, an analysis of the failure of the AEOLUS concept and its remaining potential, and the overall comparison between the different setups and those discovered in the force sensing background study in Chapter 2.3.

6.1 Requirements reflection

The most promising concept from this study is the 3-DoF ATLAS sensor. While the sensor demonstrates predictable behaviour and consistently detects force with 1 N accuracy, it does not meet the requirements defined in Chapter 3.6.2. A full pass/fail overview of all requirements is provided in Appendix B. This section reflects on the nature of those shortcomings and discusses whether the unmet requirements are strictly necessary for the intended application.

The dominant limitation of the accuracy is Hysteresis, which is investigated in Chapter 5.3. The sensor is capable of consistently detecting relative changes in force, but has issues with absolute force measurements. This can also be deducted from the results of the integration tests in Chapter 5.5

This raises an important question regarding the interpretation of the system requirements: whether absolute force measurement is strictly necessary for the intended application. As discussed in Chapter 3.2, the primary motivation for introducing force sensing is to improve spatial awareness and enable tissue differentiation. In this context, relative force changes may be sufficient. Biological tissue properties vary significantly between patients and even between different regions within the same patient (Lehmann et al., 2017).

From this perspective, the ATLAS sensor meets the functional intent behind the requirements, even though it does not satisfy the requirements. This suggests that the current requirements may be overly strict in the intended context.

6.2 AEOLUS failure analysis

The 3 DoF AEOLUS sensor did not conclude a functional prototype. As described in Chapter 4.3.4, this limitation originates primarily from the pressure loss in the air chambers. The required internal pressure of 2.3 bar is technically feasible, but the associated airflow consumption is too large in the current design. Experimental results show that the system consumes up to 340 L/min of air.

From a fundamental perspective, the AEOLUS concept suffers from an unfavourable scaling relationship. Reducing chamber size increases the required pressure, amplifying leakage flow through the system. If the leakage flow increases, the air consumption does as well.

Despite these limitations, the AEOLUS concept should not be dismissed entirely. The project focus shifted towards the ATLAS implementation, as this had a more successful 3 DoF prototype.

AEOLUS retains an advantage in system integration. Many MRI-guided robotic systems are pneumatically actuated. This allows the AEOLUS sensor to leverage existing infrastructure without requiring many additional components.

To summarise, if the pressure loss and airflow inefficiencies can be resolved, AEOLUS could become a competitive alternative due to its leverage on existing pneumatic infrastructure. However, addressing these challenges is essential before the concept can be considered viable.

6.3 Sensor comparison

The ATLAS and AEOLUS sensing concepts, together with alternative methods identified in the background study, represent fundamentally different approaches. As such, direct comparison is challenging; it would be comparing apples with pears. Each method optimises different aspects of performance, complexity, and integration.

A comparison of the investigated sensing principles is presented in Table 6.1. The comparison is based on characteristics identified throughout the literature study and experimental evaluation performed in this thesis.

Table 6.1: Comparison of different MR-safe force sensing principles.

Sensing principle	Accuracy	Complexity	MR-safety	Scalability	Main limitations
Strain gauge	High	Moderate	MR-unsafe	High	Electrical components near scanner, EMI sensitivity
Piezoelectric	Dynamic	Moderate	MR-unsafe	Moderate	Poor static force measurement, electrical interference
Capacitive	Moderate to high	High	MR-unsafe	Moderate	Sensitive to electromagnetic disturbances and alignment
FBG	Very high	High	MR-conditional	Low	Expensive interrogation hardware and complex integration
ATLAS	Moderate	Low	MR-safe	High	Hysteresis
AEOLUS	Low to moderate	Moderate	MR-saef	Moderate	Leakage sensitivity and scaling limitations

Optical sensing methods, such as Fibre Bragg Grating (FBG) systems (Moerman et al., 2013), generally offer the highest measurement accuracy and sensitivity among MR-safe sensing approaches. Additionally, optical fibres are immune to electromagnetic interference. However, these systems require complex hardware, precise alignment, and advanced signal processing. This significantly increases both implementation complexity and overall system cost. Furthermore, integration into compact robotic systems can be challenging due to fibre routing constraints and sensitivity to bending.

Conventional electrical sensing principles, such as strain gauges, capacitive sensors, and piezoelectric elements, are widely used in robotic force sensing outside MRI environments due to their high sensitivity. However, for MRI-guided applications, conductive methods may introduce electromagnetic interference, image artefacts, or safety concerns. By definition, they cannot exceed MR-conditional safety standards. They would require additional shielding and filtering, increasing integration complexity.

The ATLAS concept represents a mechanically transmitted sensing approach. The applied force is converted into a mechanical displacement that can be measured remotely outside the

MRI environment. The main strength of this approach lies in its simplicity and modularity. Most of the system can be 3D-printed, allowing rapid prototyping and straightforward integration. It is highly scalable and adaptable to different applications.

The AEOLUS concept represents a fluid-based sensing approach. Its main strength lies in its compatibility with pneumatic-driven systems. It can leverage existing infrastructure for easier integration. However, as demonstrated in this study, its performance is highly sensitive to scaling effects and leakage.

The results of this study indicate that no single MR-safe sensing principle can be considered universally optimal. Instead, the sensing method strongly depends on the application. Applications requiring highly accurate force measurements may favour optical sensing approaches despite their complexity. Applications prioritising simplicity, low cost, modularity, or rapid integration may favour approaches such as ATLAS.

7 Conclusions and Recommendations

7.1 Conclusions

The mission of this study was to "Design MR-Safe sensors to measure axial force and torques at the end effector". Multiple sensing principles were investigated, and the ATLAS sensing method showed the most promising performance. A pass/fail summary of the requirements is given in Appendix B.

The ATLAS sensing method is based on Hooke's law and estimates force through the displacement of 3D-printed spring elements. Material experiments showed that PLA-CF was the most suitable spring material due to its high effective spring constant and low drift compared to PETG and PCTG. Analytical evaluation showed that longer spring geometries increase the elastic operating range.

The resulting 3 DoF ATLAS prototype measures axial force, yaw and pitch torques using four coupled load cells. Each load cell consists of a PLA-CF spring and a Ferris-wheel mechanism to measure displacement. Tests demonstrated an axial force operating range up to 22.5 N and 0.45 Nm for torque. This is 150% of the desired operating range. The sensor achieved an accuracy of 1 N within a displacement range of ±5 mm. This does not meet the predefined medical requirement accuracy of ±0.15 N.

The primary limitation is hysteresis, originating from friction within the cable transmissions of the Ferris wheels. The friction is the root cause of the accuracy gap and is a solvable mechanical problem. The objective of force sensing in this context is to improve spatial awareness and enable tissue differentiation. As argued in Chapter 6.1, it may be achievable through relative force variation rather than absolute accuracy. Integration tests support this; the ATLAS sensor can be integrated into the MAMRI system and provide meaningful force feedback. Whether relative sensing is sufficient for safe clinical use remains an open question that should be addressed in future work, ideally in collaboration with clinical stakeholders.

In addition to the sensing principle itself, a real-time demonstration setup was developed. This setup includes live force indication and an interactive game.

The AEOLUS sensing principle was investigated as an alternative pneumatic approach. The 1 DoF proof-of-concept demonstrates the feasibility of airflow-based force sensing. However, scaling the concept to a compact 3 DoF implementation resulted in impractical airflow requirements. While no functional 3 DoF prototype was achieved due to airflow and leakage limitations, the concept remains promising for pneumatically actuated systems, as discussed in Chapter 6.2. The hydraulic POSEIDON concept was also explored, but could not be demonstrated due to unresolvable mechanical friction and was therefore discontinued.

This study establishes a structured framework for MR-safe force sensing. A modular validation framework was developed to benchmark sensing concepts without bias. Multiple sensing principles were investigated and compared using 1 DoF proof-of-concept implementations. Based on the insights gained, a 3 DoF sensor was designed for the MAMRI end effector and its integration was evaluated. A real-time indication method, including an interactive demonstration, was developed to illustrate the sensor's capabilities.

In conclusion, this study demonstrates that MR-safe force sensing can be achieved using simple and accessible principles. The 3 DoF ATLAS force sensor provides a simple and functional solution. This establishes a strong foundation for further development of practical MR-safe sensing systems.

7.2 Recommendations

Two main directions for future work are identified: further development and exploration. The first direction focuses on advancing the current sensing concepts. In particular, efforts should be directed towards reducing hysteresis effects, as this remains the dominant limitation in measurement accuracy. Improvements to the Ferris wheels or the introduction of alternative low-friction mechanisms may significantly enhance performance. Alternatively, investigating the AEOLUS sensing method could provide insight into whether similar MR-safe principles can achieve higher accuracy and improved repeatability. Both of which aim to bring the sensor performance closer to medical requirements.

The second direction involves exploring the ATLAS sensing principles in a wider range of applications. Sensor performance depends on mechanical design, and different applications impose varying accuracy and sensitivity requirements. Adapting the concept to specific use cases may therefore result in more effective and application-driven implementations.

Potential applications can be both software- and hardware-oriented projects. On the software side, one application is the implementation of force control for the MAMRI arm, enabling adaptive path planning when the path is obstructed, improving patient safety. Another possibility is the integration of force feedback into a user interface, improving operator awareness during procedures. These applications can be realised using the current hardware configuration, including the 3 DoF ATLAS sensor.

On the hardware side, a promising direction is the integration of the ATLAS sensing principle with pneumatic actuators, enabling the development of a motor with embedded torque feedback. Such a system could be used to detect missed steps and reconstruct interaction forces through kinematic models. These examples illustrate that the applicability of the sensing principle extends beyond the current implementation and can be adapted to a wide range of systems.

A Demo Manual

The ATLAS demo is an interactive game designed for Open Days and other technical events at the University of Twente. The objective of the game is to use the force sensor as a joystick to collect as many randomly placed dots on the screen as possible. Each player is given 30 seconds, and a high score system is used to track performance. This setup provides an engaging way to initiate conversations about the project and the underlying technology.

The system has the following external requirements:

- An IoTroam (eduroam) network connection
- 5 V power supplied via USB-C (e.g., a phone charger or laptop)
- A laptop to access the interface website
- A glue clamp to fix the setup to the table

A.1 Standard Use

The demo setup is contained within a single box. Including: the Ferris wheel assembly with electronics, the ATLAS sensor, and the end effector with plastic bolts. To set up the demo, follow the steps below:

1. Place all components on a stable table.
2. Secure the ATLAS base to the table using a glue clamp.
3. Screw on the end effector on top of the ATLAS sensor.
4. Mount the tubes of the ATLAS sensor onto the sides of the Ferris wheels by matching the lengths indicated by the black tape markings (long to long, short to short). A slit is provided on the side for the rope to pass through.
5. Connect the ropes from the ATLAS tubes to the ropes from the Ferris wheels by hooking the 3D-printed connectors together.
6. Provide power to the setup by connecting a USB-C cable with a 5 V power (e.g., via a phone charger or laptop).
7. The OLED screen will display a booting message. After initialisation, an IP address should be shown. If an error occurs, refer to Chapter A.2.
8. Ensure that the laptop is connected to eduroam or eduvpn.
9. Enter the displayed IP address into a web browser. The interface has been tested with Chrome, but should function on most modern browsers.
10. In the web-app, press the "Game on" button.
11. The system is now ready for use. Have Fun!

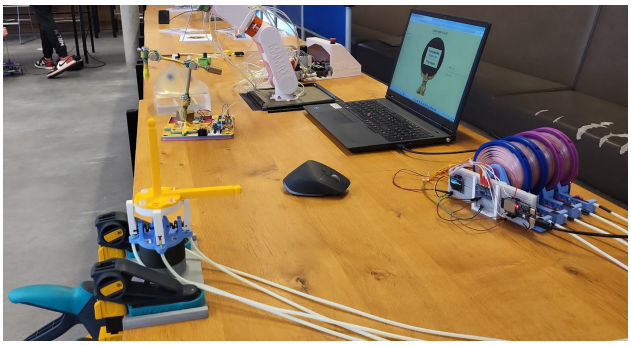


Figure A.1: The Demo Setup

Note: If the setup exhibits stick drift, press the reset button on the ESP32 to recenter the sensor.

A.2 Common Errors

If an issue occurs, it may result in unexpected behaviour (Section A.2.1) or a system error. In the event of an error, an error code will be displayed on the OLED screen. Table A.1 provides an overview of the error codes, their meaning, and possible solutions. As a reference, the electrical circuit in Figure A.2 shows the correct connections.

Table A.1: Error Codes

Error code	Description	Solution
TCA_NOT_FOUND	Unable to connect to the I2C multiplexer	Check the I2C cables connected to the TCA multiplexer
FW_RE_CH_[number]	Ferris wheel read error at channel [number]	Check the I2C connection to the Ferris wheel at the specified channel on the multiplexer
FATAL_ERROR	Unspecified critical error	Contact Antonie Veldwachter or Vincent Groenhuis

A.2.1 Strange Behaviour

- **Unresponsive or bad responsive behaviour**
  This is usually caused by an unstable network connection. The issue may resolve automatically; if not, press the reset button on the ESP to re-establish the connection. Refreshing the webpage may also resolve the issue.
- **Stick drift**
  Over time, the sensor may drift, causing the dot to move slowly in one direction. Press the reset button on the ESP to re-centre the sensor. This calibration is also performed automatically during startup.
- **Asymmetric behaviour**
  In some cases, motion in one direction may appear less responsive than in another direction (up/down, left/right). This is typically a hardware issue. Check the tube connections of the Ferris wheels, as one is probably disconnected.

A.3 Electrical circuit

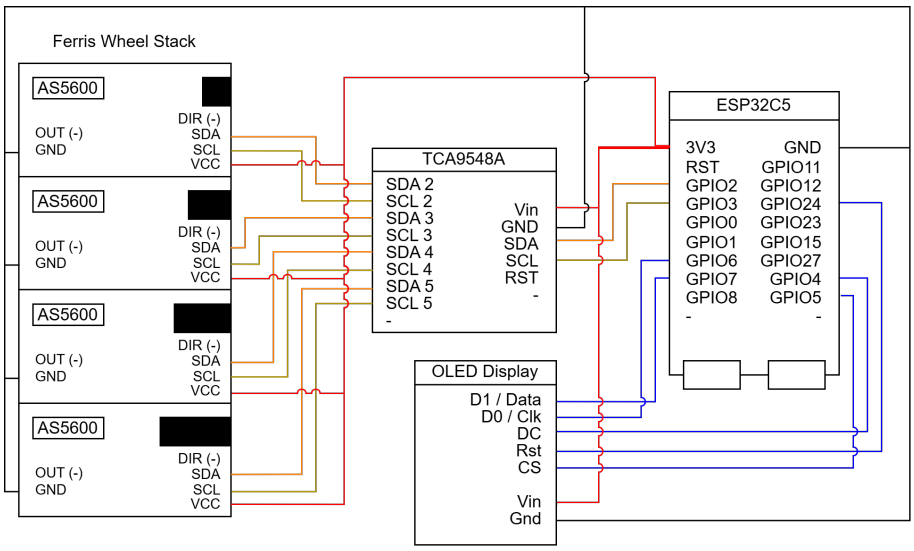


Figure A.2: Demo Electrical Circuit

B Pass/Fail Summary

This study resulted in the development of the 3 DoF ATLAS sensor. Returning to the system requirements defined in Chapter 3.6, each relevant requirement was evaluated based on the test results presented in Chapter 5. Table B.1 summarises the overall requirement evaluation.

Table B.1: Pass/Fail Summary for 3 DoF ATLAS

Nr.	Requirement	Value	Pass/Fail
SR01.01	The sensor must be modular to allow integration in different systems.	-	Pass
SR01.02	The sensor must be plug-and-play, requiring minimal setup.	-	Pass
SR01.04	The sensor must be MR-safe.	-	Pass
SR01.05	The system must have a digital output for easy integration	-	Pass
SR01.08	The system should provide an intuitive display for real-time force/torque measurements.	-	Pass
TR01.01	The sensor must measure axial forces within the desired range.	[−15 N, 15 N]	Pass
TR01.02	The sensor must measure axial force with an accuracy of ±1% of full scale.	±0.15 N	Fail
TR01.03	The sensor must have a resolution better than 0.1 N.	< 0.1 N	Fail
TR01.04	The sensor must tolerate forces up to 150% of full scale.	≤ 22.5 N	Pass
TR01.05	The sensor should have a maximum total travel of ±5 mm	±5 mm	Pass
TR02.01	The sensor must measure torque in both directions within the desired range.	[−0.3 Nm, 0.3 Nm]	Pass
TR02.02	The sensor must measure torque with an accuracy of ±5% of full scale.	±0.015 Nm	Fail
TR02.03	The sensor must have a resolution better than 0.01 Nm.	< 0.01 Nm	Fail
TR02.04	The sensor must tolerate forces up to 150% of full scale.	≤ 0.45 Nm	Pass
TR02.05	The sensor should have a maximum total travel of $\pm 5^o$	±5°	Pass
TR03.01	The system must provide measurements with sufficient sampling frequency for real-time feedback.	≥ 5 Hz	Pass
TR03.02	The sensor must stay within the MAMRI end-effector circular footprint	$\phi \leq 64$ mm	Pass
TR03.03	The indication (display/interface) should reflect sensor data with minimal latency.	< 100 ms	Pass
TR03.04	The sensor should have a modular interface.	-	Pass
TR03.05	The system should include a straightforward calibration procedure to account for drift or setup changes.	-	Pass

C The 1 DoF ATLAS

***A**ngular **T**orsion **L**oad **A**cquisition **S**ensor*

C.1 Description

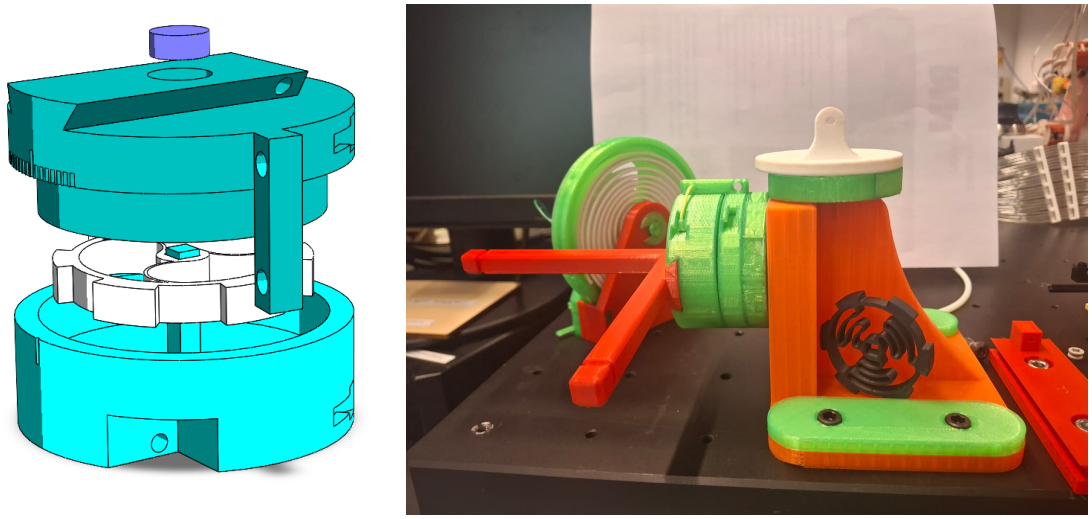
According to Hooke's law (Equation C.1), the force exerted by a spring can be determined from its stiffness and deformation. The ATLAS uses this principle to measure forces applied at the robot's end effector.

$$F = k \times x \tag{C.1}$$

The system consists of two main components. The first component, mounted on the robot's end effector and shown schematically in Figure C.1a, consists of two disks connected by a rotational spring. When an external force is applied, the disks rotate relative to one another. This relative rotation is transferred via a tensioned string.

The second component maintains this string tension. It is a pre-tensioned wheel connected to the string, whose rotation is measured using a Hall-effect encoder. The wheel's rotational position corresponds directly to the relative displacement of the rotational spring, and therefore to the force acting on the end effector.

The complete experimental setup is shown in Figure C.1b.



(a) Schematic Endeffector

(b) Real Setup

Figure C.1: The ATLAS

C.1.1 Tuning

The stiffness of the spring determines both the operating range and the measurable force range of the sensor. Designing a 3D-printed spring with a precise spring coefficient is challenging, as it depends on print quality, material properties, and geometric accuracy. Simulations can provide estimates of the spring constant, but these often deviate from real-world behaviour.

The most reliable tuning procedure is therefore:

1. **Design an initial spring geometry**
   Longer blades generally produce more compliant and robust springs. The geometry should primarily constrain motion to a single degree of freedom.
2. **Measure the current spring coefficient**
   Apply calibrated weights and use Hooke's law (Equation C.1) to determine the spring constant experimentally.
3. **Adjust the spring thickness to reach the desired stiffness**
   Because the thickness has the strongest influence on stiffness, it is the primary tuning parameter.

Relationship Between Thickness and Spring Coefficient

For a leaf spring approximated as a cantilever beam, the tip deflection under a force F is given by

$$x = \frac{Fl^3}{3EI}, \tag{C.2}$$

where the second moment of area of a rectangular cross-section is

$$I = \frac{bt^3}{12}. \tag{C.3}$$

The variables are defined as:

- E: Young's modulus (material-dependent),
- I: second moment of area,
- F: applied force,
- l: beam length,
- b: beam width,
- t: beam thickness.

Substituting I and solving for the spring coefficient yields

$$k = \frac{F}{x} = \frac{3EI}{l^3}, \tag{C.4}$$

$$k = \frac{Ebt^3}{4l^3}. \tag{C.5}$$

If material, width, and length remain constant, the spring coefficient depends solely on the cube of the thickness.

Adjusting to the Desired Spring Coefficient

To modify the spring coefficient from a current value k_{current} to a desired value k_{desired}, the required thickness is

$$t_{\text{desired}} = t_{\text{current}} \times \sqrt[3]{\frac{k_{\text{desired}}}{k_{\text{current}}}}. \tag{C.6}$$

This cubic relationship makes thickness an effective and predictable tuning parameter for 3D-printed leaf springs.

C.2 Tests

This chapter adds to Chapter 5 by providing additional details on the tests and by presenting the full set of measurement results. The purpose of this appendix section is purely descriptive; interpretation and conclusions drawn from these experiments are addressed in the main body of the report.

C.2.1 Material Tests over Time

Setup

Based on the initial analysis in Chapter 3, three printable materials were selected for testing: PLA-CF, PETG, and PCTG. Each material is evaluated under identical loading conditions, using springs of equal geometry and thickness. The spring geometry is shown in Figure C.2. The only variable between the tests is the spring material itself.

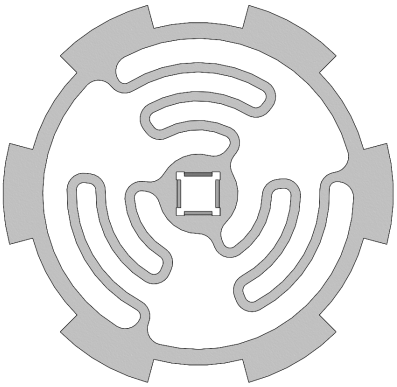


Figure C.2: Spring Geometry

The springs are mounted in the experimental setup shown in Figure C.1. A mass of 500 g is suspended from the lever arm, producing a constant downward force at the end of the lever and, consequently, a torque applied to the spring. This load is maintained for 3 to 5 days, during which measurements are taken daily to quantify material drift over time.

The drift is expressed in degrees (per day), as the Ferris wheel mechanism, described in Section 4.2.3, measures the absolute rotational position of the system.

Results

Table C.1: Measured material drift under constant load

Material	Drift (deg/day)
PLA-CF	0.20
PCTG	0.43
PETG	1.10

Among the tested materials, PLA-CF exhibits the lowest drift over time. However, due to its lower cost and improved printability, PCTG is also considered a viable candidate for further development. After completion of the tests, the springs were compared to an identical, untested reference set in order to assess potential plastic deformation. No significant plastic deformation was observed on the exterior of any of the tested springs.

C.2.2 Spring Constant for Different Materials

Setup

To further investigate the material-dependent spring characteristics, PCTG and PLA-CF (carbon fibre–reinforced PLA) were tested for their effective spring constants. The experimental configuration remains identical to the setup shown in Figure C.1.

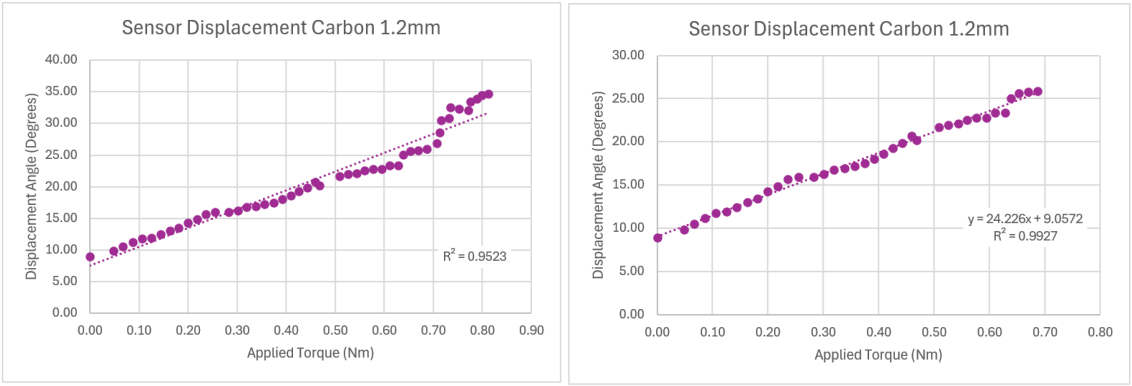
Calibrated weights are applied to the lever arm in increments of predominantly 20 g, covering a total range from 0 to 1000 g. For each applied load, the angular position of the Ferris wheel is recorded and plotted as a function of the applied force. In this experiment, an angular displacement of 0 degrees corresponds to the lever being in a perfectly horizontal position.

To minimise the influence of hysteresis, a brief downward preload is applied to the rope suspending the weights before each measurement. This ensures that the springs consistently pull the system back in the same direction, thereby subjecting the mechanism to hysteresis in a controlled and repeatable manner.

Results

The PLA-CF springs were tested first. After completion of the experiment, it was observed that the PLA axial shaft passing through the spring and directly connected to the outer lever had bent. This indicates that plastic deformation occurred in the axial component during testing.

Inspection of the measurement data, shown in Figure C.3a, reveals that this plastic deformation becomes apparent at an applied torque of approximately 0.7 Nm. Consequently, all measurement points above this torque level are excluded from further analysis.



(a) PLA-CF with plastic deformation

(b) PLA-CF without plastic deformation

Figure C.3: PLA-CF spring test results

Figure C.4 shows the PCTG results of the test, and Figure C.5 shows the PETG results.

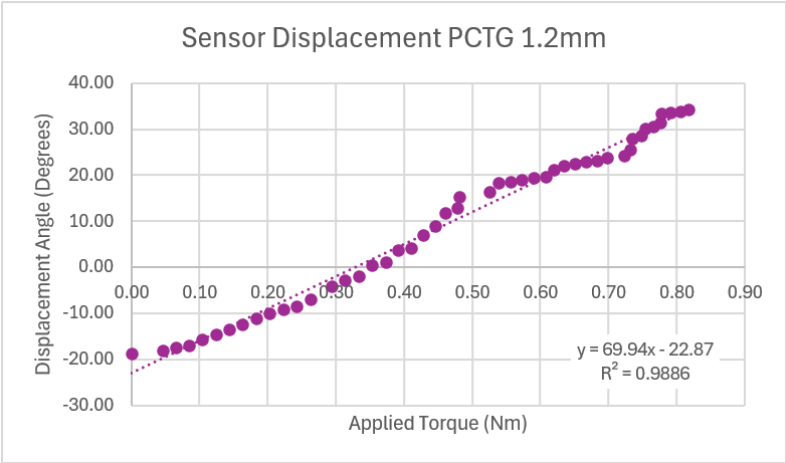


Figure C.4: PCTG spring test results

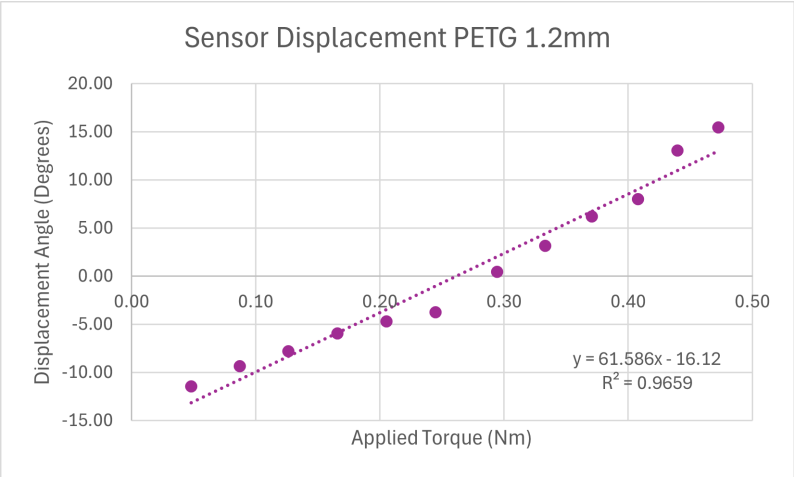


Figure C.5: PETG spring test results

For visual comparison, the most promising spring materials (PCTG and PLA-CF) under load are shown side by side in Figure C.6.

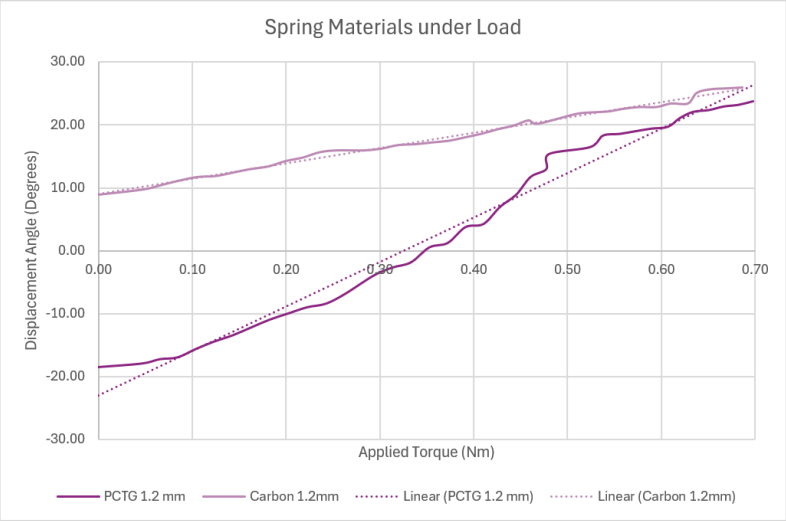


Figure C.6: Spring materials under load

Overall, the PLA-CF springs exhibit a higher and more consistent effective spring constant compared to the PCTG springs. Their effective spring constants are shown in Table D.1

Results

Table C.2: Effective Spring Constant of Different Materials

Material	Effective Spring Constant (Nm/deg)
PLA-CF	0.041
PCTG	0.014
PETG	0.016

The effective spring constants shown in Table C.2 were determined using linear fits on the data. All fitted models resulted in R^2 values above 0.96, indicating linear spring behaviour within the tested range.

D The 3 DoF ATLAS

*Angular **T**orsion **L**oad **A**cquisition **S**ensor*

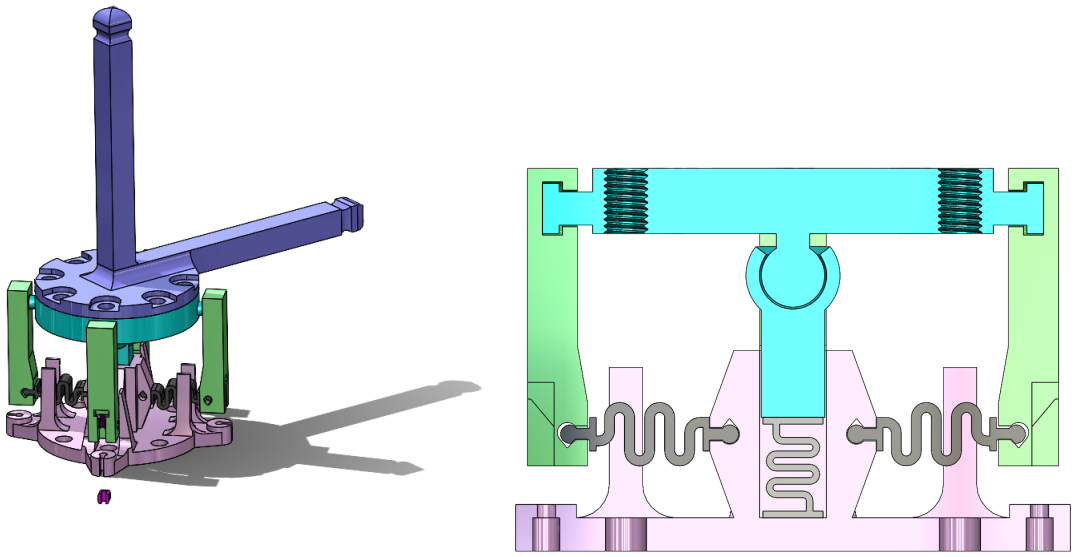
D.1 Description

Similar to the 1 DoF version, the 3 DoF ATLAS estimates applied forces using Hooke's law (Equation C.1). The measurement principle remains unchanged; however, this version extends the concept by employing multiple coupled springs to measure forces acting in three degrees of freedom.

$$F = k \times x \tag{D.1}$$

The sensor consists of four mechanically coupled load cells arranged symmetrically around a central column. In the 1 DoF ATLAS, small amounts of mechanical play were introduced by the interfaces between different materials, which negatively affected measurement accuracy. To address this limitation, the 3 DoF ATLAS incorporates a mechanically interlocked design using a central spring column, effectively constraining relative motion and reducing compliance-induced errors.

This interlocking mechanism is clearly visible in the cross-sectional view shown in Figure D.1b. Each of the four arms is equipped with a Ferris wheel mechanism (see Section 4.2.3) to measure the displacement of its corresponding spring element. The spring and measurement together create a load cell. By combining all four load cells, the sensor estimates external forces acting on the end effector in three degrees of freedom.



(a) Side View **(b)** Cross Section

Figure D.1: The 3 DoF ATLAS

D.2 Calibration

D.3 Tests

This chapter serves as a supplement to Chapter 5. It provides a more detailed description of the experimental setups and presents the complete set of obtained results. No new analysis or conclusions are drawn in this chapter, as these are discussed in the main body of the report.

D.3.1 Axial Force

Setup

To measure the axial force, a controlled load is applied using the validation framework described in Section 4.1. This framework ensures that the applied force is aligned with the sensor's axial direction. The complete experimental setup is shown in Figure D.2.



Figure D.2: ATLAS axial force test setup

The force is applied by placing calibrated weights at the end of a horizontal lever arm. A spirit level mounted on top of the lever is used to ensure horizontal alignment during the measurements. The weights are positioned at a distance of 300 mm from the lever's rotation point, while the centre of the ATLAS sensor is located 123 mm from this rotation point. As a result, the force applied at the end of the lever is amplified by a factor of 2.44 when transmitted to the sensor.

During the experiment, the software computes the amount of rope unspooled from the disks, based on their known radius of 51 mm. Weights ranging from 0 to 1000 g are applied at the end of the lever, primarily in increments of 20 g. The sensor is calibrated without the lever-arm resting on it; the arm itself weighs 84 g and is added to the applied force.

To improve repeatability and consistency of the measurements, a small downward preload is briefly applied to the rope before each measurement. This ensures that the springs always pull the system back in the same direction, thereby subjecting the Ferris wheel mechanisms to hysteresis in a consistent manner and reducing measurement variability.

Results

To structure the measurement data, the four load cells are referenced using a compass-based convention. With respect to the orientation shown in Figure D.2, the *North* load cell is located on the right-hand side of the sensor, *East* faces toward the camera, *South* is positioned on the left-hand side, and *West* faces away from the camera. The axial force response of each load cell is shown in Figure D.3.

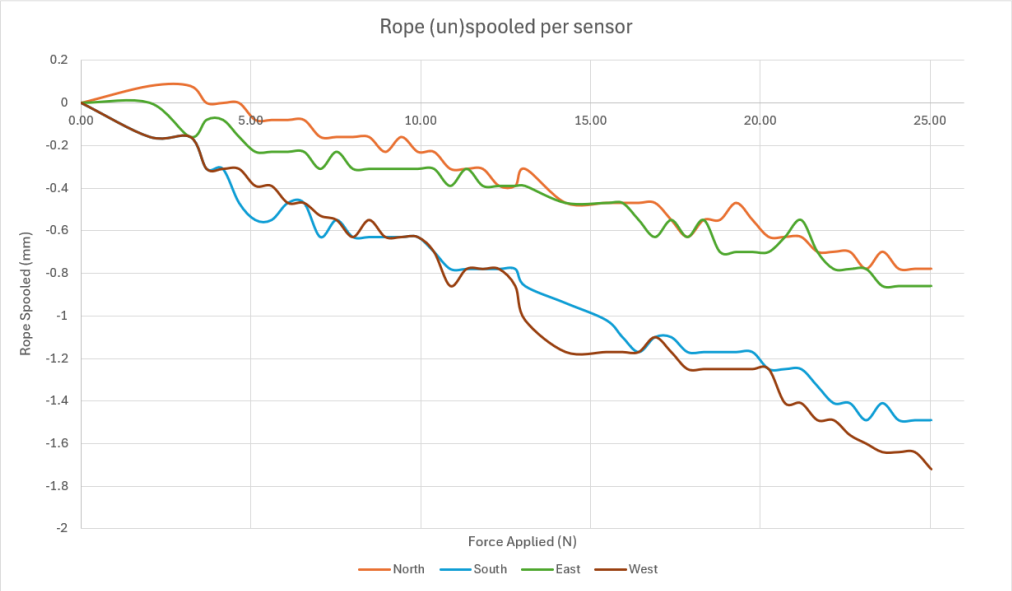


Figure D.3: Axial force response per load cell

When compared to a linear trend line, all load cells exhibit an R^2 value above 0.985, indicating a predominantly linear response and allowing the remaining inconsistencies to be treated as white noise. To combine the measurements of the four load cells, the average displacement is computed for each applied force. This average rope displacement is then used to estimate the effective spring constant of the system using Hooke's law, expressed as

$$k = \frac{\Delta F}{\Delta x}. \tag{D.2}$$

Using this relation, the compliance and corresponding spring constants of the system are obtained as listed in Table D.1.

Table D.1: Estimated compliance and spring constants for axial force loading

	Compliance (mm/N)	**Spring Constant (N/mm)**
Average	-0.049	-20.492
North	-0.030	-33.898
East	-0.034	-29.762
South	-0.064	-15.723
West	-0.069	-14.599

Figure D.4 compares the averaged measured displacement of the ATLAS sensor with the displacement estimated using the identified spring constant, the applied force, and Hooke's law.

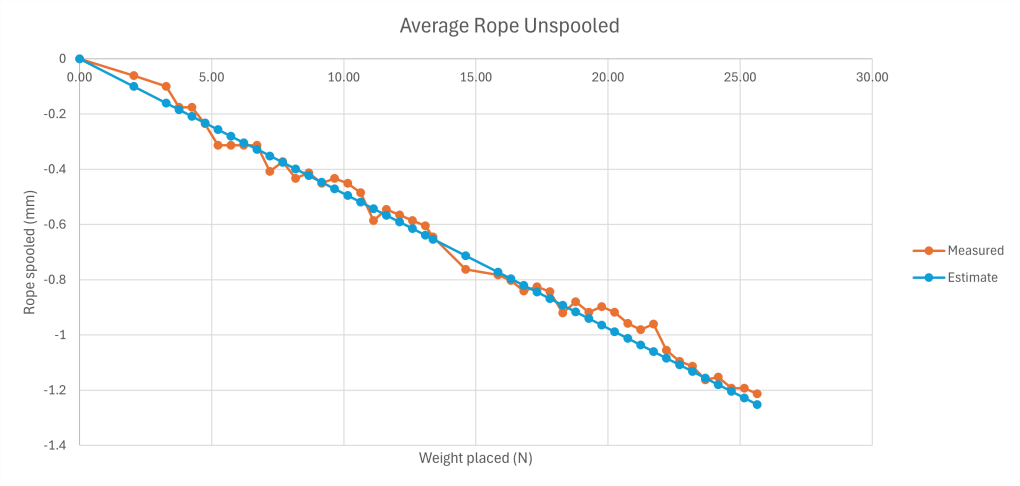


Figure D.4: Average displacement of the ATLAS sensor under axial force

The resulting dataset exhibits an R^2 value of 0.998, indicating a very close agreement between the measured data and the linear model. The found accuracy, defined to be 2 standard deviations of the absolute error, was 1.1 N.

D.3.2 Drift tests

Setup

The same setup as shown in Figure D.3 was used. For this test, a mass of 0.5 kg was suspended from the rope for one week. The system state was recorded throughout the week. Drift per day was calculated by dividing the total change in each measured quantity by the elapsed time in days.

Results

Table D.2 shows the measured force and directional displacements over the test period. The average daily drift was computed based on all measurements.

Table D.2: Measured directional displacement and applied force.

Day	Force	North	South	East	West
10 Feb '26	8.89 N	-0.63 mm	-0.23 mm	-0.23 mm	-0.55 mm
11 Feb '26	8.89 N	-0.63 mm	-0.23 mm	-0.23 mm	-0.55 mm
12 Feb '26	9.14 N	-0.63 mm	-0.23 mm	-0.23 mm	-0.63 mm
16 Feb '26	10.1 N	-0.78 mm	-0.39 mm	0.47 mm	-1.33 mm
17 Feb '26	9.97 N	-0.70 mm	-0.39 mm	0.63 mm	-1.41 mm
Average	0.12 N/day	-0.008 mm/day	-0.012 mm/day	0.060 mm/day	-0.073 mm/day

D.3.3 Yaw and Pitch Single-Cell Torque

Setup

The yaw and pitch axes are aligned directly above the springs. The yaw axes is measured by the North and South load cells and the pitch is measured by the East and West load cells. In this configuration, two springs primarily measure yaw torque, while the other two measure pitch torque. By positioning the lever over the springs, as illustrated in Figure D.5, a pure yaw or pitch torque can be applied. This arrangement ensures minimal coupling between the two rotational degrees of freedom.



Figure D.5: ATLAS Torque Test Setup

Results

The measured yaw and pitch responses are consistent with the expected behaviour. For both degrees of freedom, the North and South (East and West for pitch) outputs show mirrored responses, confirming symmetric loading of the structure. The opposite poles during the tests remained at 0.

To improve force reconstruction accuracy, the signals from the two opposing poles are combined using their absolute average. The bundled response is included in the presented graphs. The found accuracy at two standard deviations was 0.071 Nm for the torque response and 0.124 Nm for the pitch response.

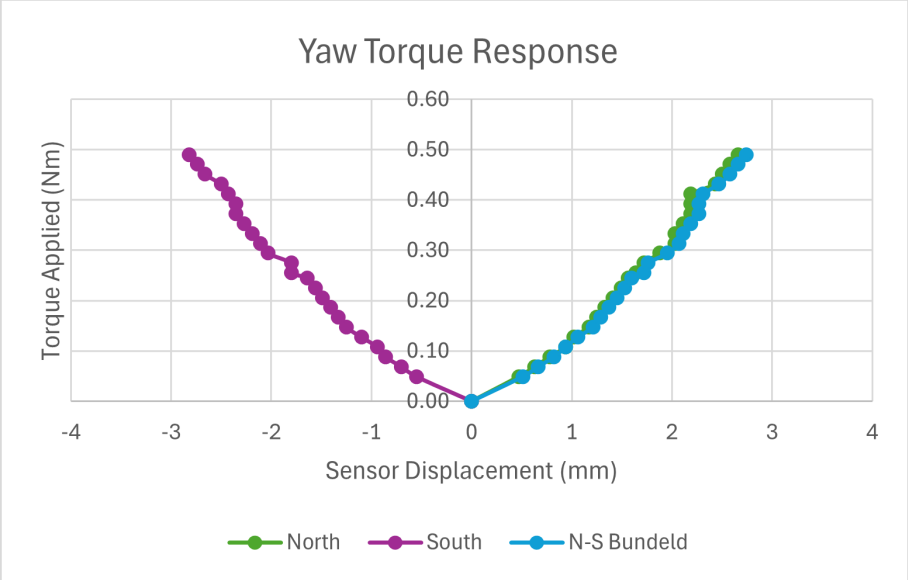


Figure D.6: Single DoF Yaw Response

D.3.4 Dual-Cell Torque

Setup

To improve measurement accuracy, it is hypothesised that using multiple load cells to measure a single degree of freedom would reduce noise and increase robustness. Instead of aligning the rotational axis directly above individual load cells, the axis is defined between two load cells. In this configuration, all four load cells would contribute to measuring a single degree of freedom in a coupled manner.

For this experiment, the load was applied between the South and East load cells. The remainder of the setup is identical to the configuration shown in Figure D.5.

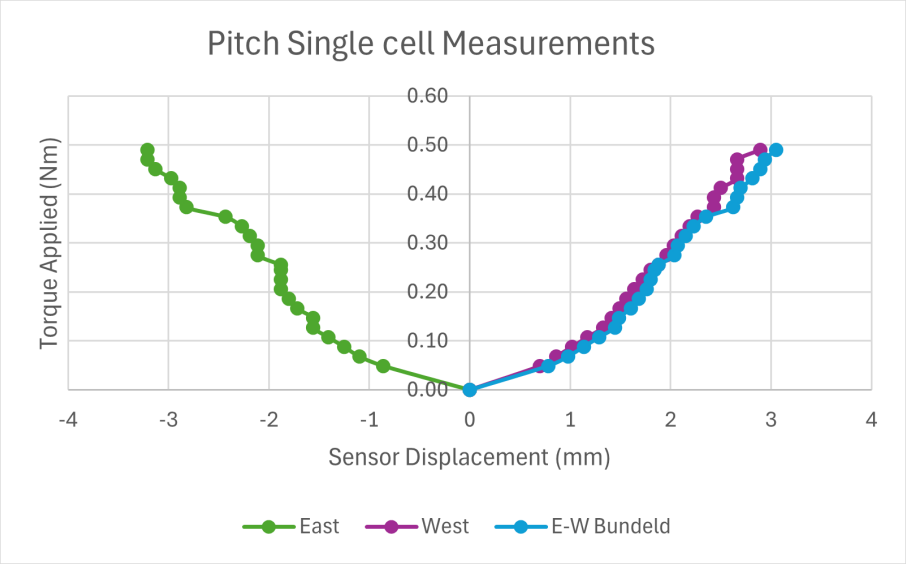


Figure D.7: Single DoF Pitch Response

Results

The results of the dual-cell torque test are shown below. The achieved accuracy was 0.066 Nm, representing only a marginal improvement over the previously obtained accuracy of 0.071 Nm. Therefore, the benefit of the dual-cell configuration appears limited under the tested conditions.

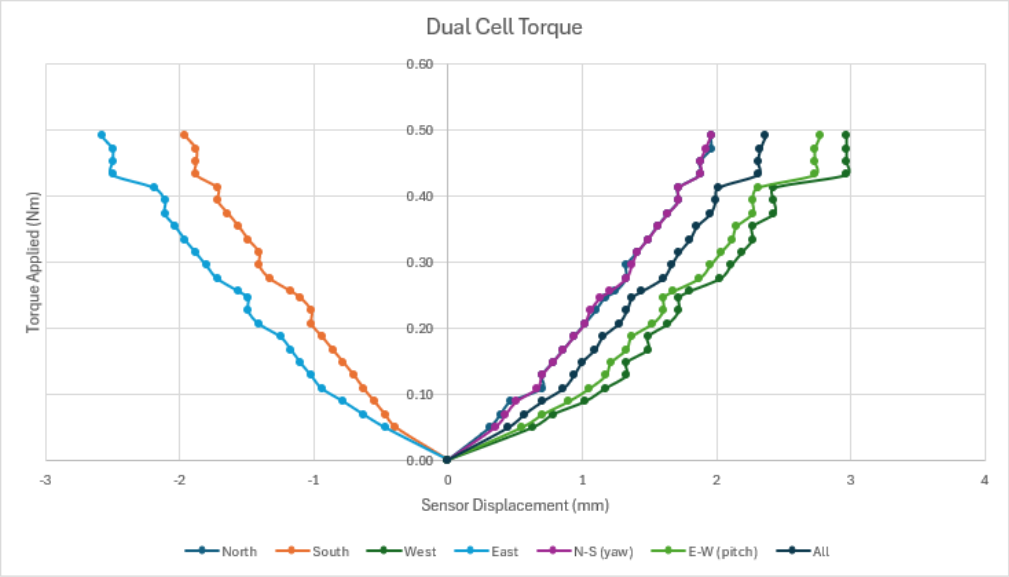


Figure D.8: Dual DoF Response

D.3.5 Hysteresis tests

Setup

For the hysteresis test, the system was placed in a controlled environment. A 1 kg mass was used to generate the push force, while the base of the system beneath the sensor was weighted to 1.5 kg. The system was calibrated using the calibration software before testing.

Calibration established a zero reference by approaching the equilibrium position from both directions: From below (after compression) and from above (after applying a tensile load). This procedure ensured a consistent and repeatable zero reference.

The hysteresis test evaluated the response when approaching this zero position from both compression (push) and tension (pull). For the push response, a 1 kg mass was placed on top of the sensor, removed, and the displacement relative to the zero reference was recorded. For the pull response, the 1.5 kg system was lifted and then placed back on the ground, after which the displacement from zero was measured.

This procedure was repeated for 15 iterations for both push and pull conditions.

Results

The hysteresis results are shown in Figure D.9.

The North and South cells exhibit a relatively stable hysteresis band of approximately 0.3 mm. In contrast, the East and West cells show larger variability and less consistent behaviour.

The results suggest that hysteresis is influenced by multiple factors beyond compression magnitude alone. The loading rate and system orientation appear to affect the response, contributing to variability and reducing predictability.

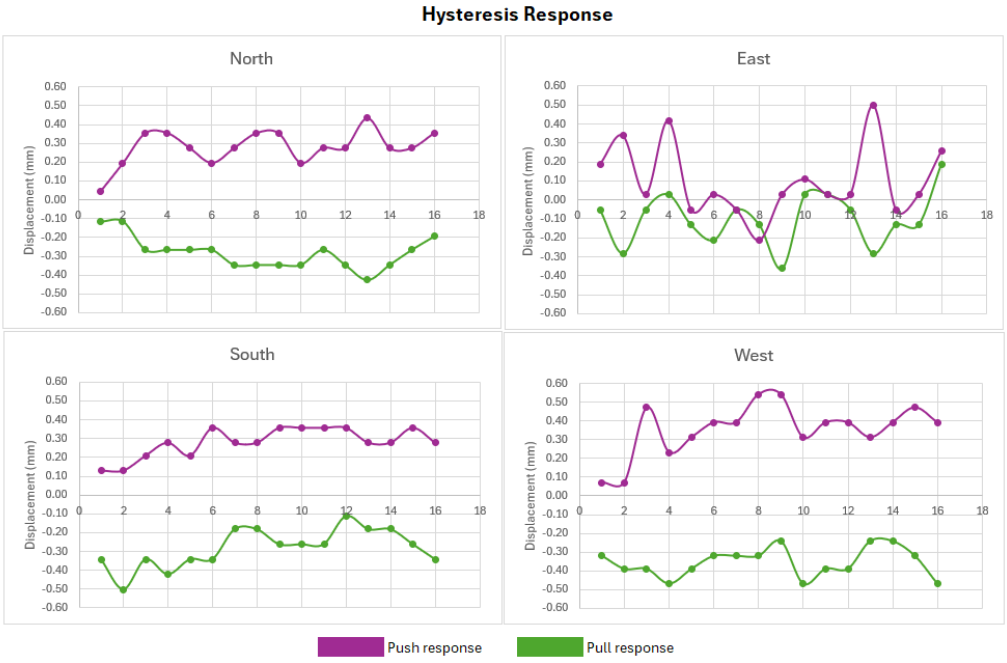


Figure D.9: Hysteresis Response per Cell

D.4 Data Sheet

Table D.3: Axis Definition

Force	Positive Direction Definition
Axial Force F_z	Downward force (compression on all load cells)
Yaw Torque τ_y	Clockwise rotation (East compression, West extension)
Pitch Torque τ_p	Forward rotation (North compression, South extension)

Table D.4: Found Accuracies

Force	Accuracy (2σ)	Spread (3σ)
Axial Force	±1.1 N	±1.79 N
Yaw Torque	±0.103 Nm	±0.123 Nm
Pitch Torque	±0.124 Nm	±0.276 Nm
Dual Cell Torque	±0.067 Nm	±0.095 Nm

Table D.5: Hysteresis Behaviour

Hysteresis Description	North	South	East	West
Average Error	0.28 mm	0.28 mm	0.10 mm	0.35 mm
Max Spread	0.86 mm	0.86 mm	0.86 mm	1.01 mm
2σ value	0.60 mm	0.60 mm	0.39 mm	0.75 mm

Table D.6: Creep Behaviour

Creep Description	Value
Average Creep	0.12 N/day
North	0.008 mm/day
South	0.012 mm/day
East	0.059 mm/day
West	0.073 mm/day

Table D.7: Spring Constants

Force	Effective Spring-constant
Axial Force	−20.49 N/mm
Yaw Torque	0.185 Nm/mm
Pitch Torque	0.193 Nm/mm

E The 1 DoF AEOLUS

***A**irflow **E**ncoded **O**utput for **L**oad-**U**tility **S**ensing*

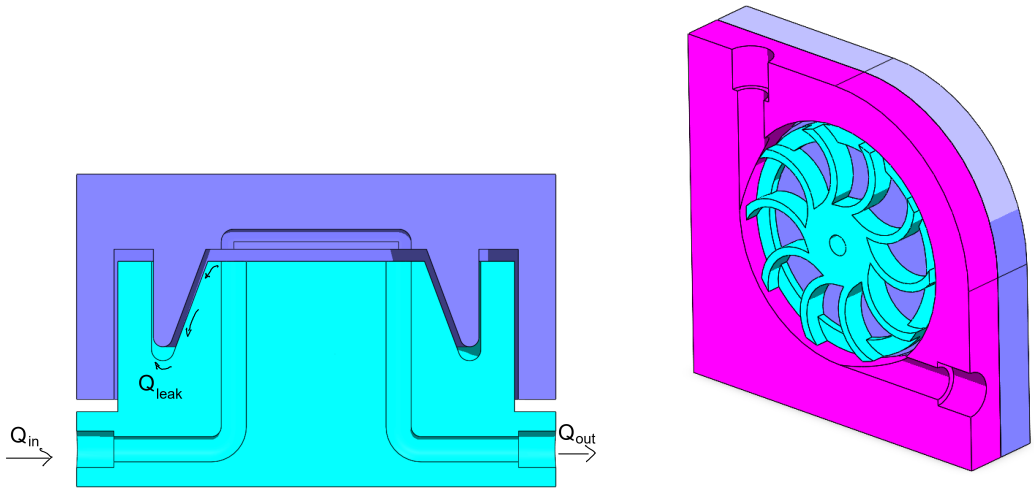
E.1 Description

The AEOLUS sensor uses airflow as both a compliant element and a means of measuring applied force. The end effector contains an air pocket inside a tubular housing.

In the unloaded state, the air pocket expands until it reaches a mechanical end stop, at which point the internal pressure is minimal and only a small amount of air flows through. Under increasing external load, the air pocket compresses and the leakage path closes, forming a continuous channel through the tube. In this fully compressed state, the airflow velocity increases significantly. A schematic cross-section of the end effector is shown in Figure E.1a.

The airflow is measured within the control room of the MRI. The returning airflow of the end effector is measured using an airflow sensor (Figure E.1b). This sensor features a small wheel driven by the air stream and mechanically coupled to a DC motor, which acts as a generator. The voltage generated by the motor is proportional to the airflow rate, and therefore to the applied force.

The force range of the AEOLUS can be tuned by adjusting the input air pressure. Higher inlet pressures increase the stiffness of the pneumatic “spring” and thereby raise the maximum measurable force.



(a) End Effector Crosscut **(b)** Flow Sensor Crosscut

Figure E.1: AEOLUS Design

E.2 Force to Output Voltage Test

E.2.1 Setup

For this experiment, the AEOLUS sensor is mounted in its intended operational configuration, with the pneumatic input connected to the laboratory pressurised air supply. The supply pressure is regulated to 2.5 bar. External loads are applied by placing calibrated weights on top of the sensor, with total masses ranging from 1000 g to 1500 g.

This mass range is selected because a minimum load is required to overcome the pneumatic pressure acting on the system. The applied weight is increased in increments of 40 g, allowing the load to be distributed symmetrically and ensuring that a predominantly axial force is applied without introducing additional torque.

At each load level, the output voltage generated by the DC motor is measured and recorded. Measurements are performed under two electrical conditions: an open-circuit configuration and a closed-circuit configuration, in which a diode is used to create an effective short circuit. The complete experimental setup is shown in Figure E.2.

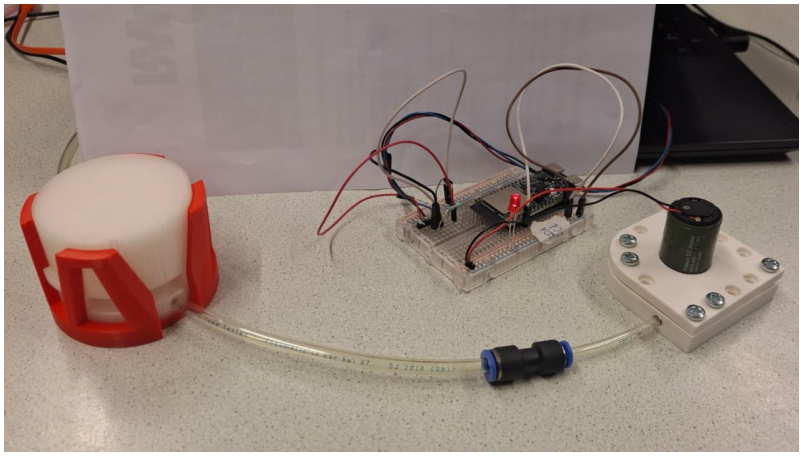


Figure E.2: The AEOLUS test setup

Results

The measurement results for both electrical configurations are presented below. It should be noted that the underlying relationship between applied force and generated voltage is exponential over the full operational range. However, within the limited physical displacement range explored in this experiment, the response can be well approximated as linear.

Additionally, when the system operates in the open-circuit configuration, the DC motor requires a relatively long settling time, approximately 60 seconds, to reach equilibrium. Which would be too long for the design constrains.

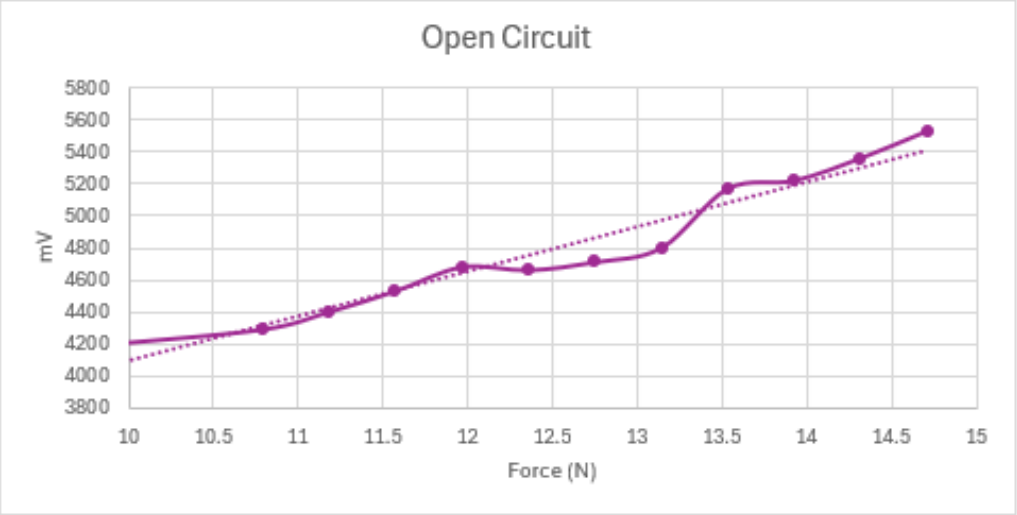


Figure E.3: AEOLUS in open-circuit configuration

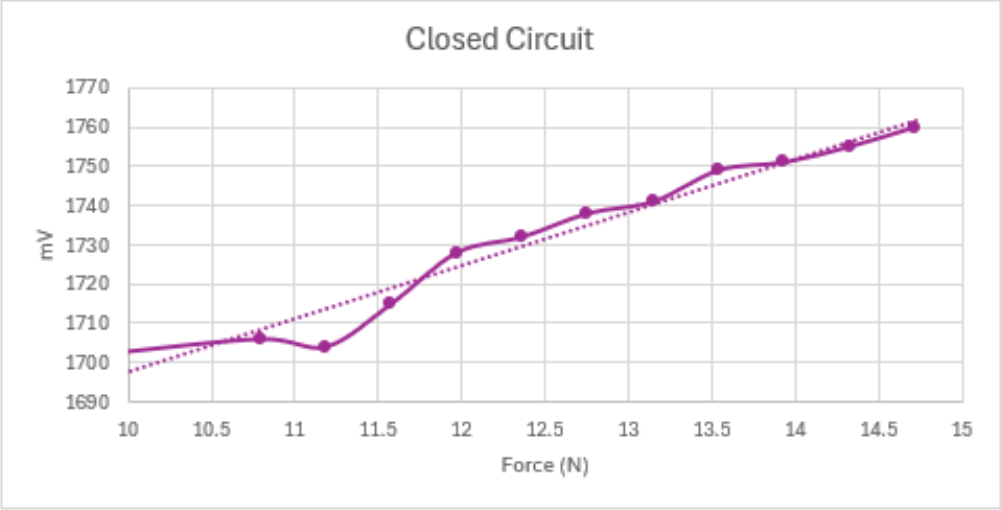


Figure E.4: AEOLUS in closed-circuit configuration

F The 3 DoF AEOLUS

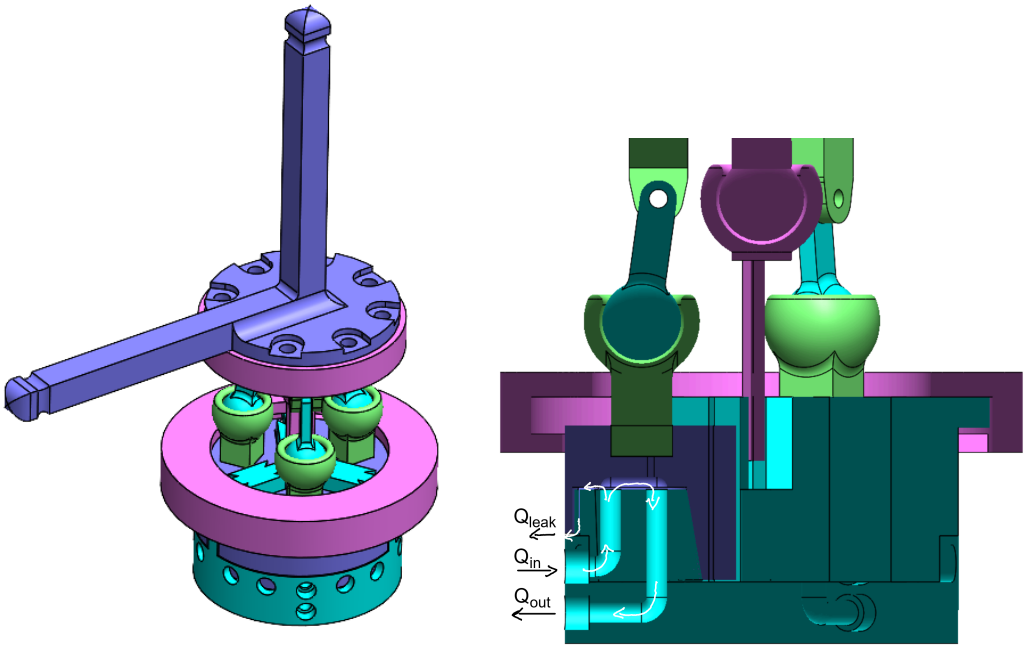
***A**irflow **E**ncoded **O**utput for **L**oad-**U**tility **S**ensing*

F.1 Description

Similar to the 1 DoF version, the AEOLUS sensor measures force through airflow. The underlying concept and flow sensor design remain unchanged (see Appendix E.1). The primary difference in the 3 DoF design lies in the subdivision of the air chamber.

To enable three DoF measurements while maintaining a compact and modular footprint, the single air chamber is divided into three mechanically coupled chambers. Each chamber has its own inlet and outlet for pressurised air. The coupling between the chambers allows the system to reconstruct three force components from their relative responses.

The design is shown in Figure F.1.



(a) Side View **(b)** Cross Section

Figure F.1: The 3 DoF AEOLUS

F.2 Air Usage Tests

Although the 1 DoF sensor demonstrated promising behaviour, this performance does not directly scale to the 3 DoF design. The reduced chamber volume introduces significant pressure losses, as also discussed in Section 4.3.4. Additionally, the current flow sensors (Section 4.3.2) could not overcome static friction, making them unable to measure the forces within this system.

This experiment aims to quantify the actual airflow consumption of the 3 DoF AEOLUS sensor.

F.2.1 Setup

An air compressor with a known tank volume is used to estimate the airflow through the sensor. The sensor inlet is directly connected to the compressor, while the outlet is connected to the

flow sensors. Although these sensors do not produce measurable output under these conditions, they provide a realistic representation of the output resistance.

F.2.2 Method

The compressor tank is initially pressurised to 6 bar. Upon opening the valve, air flows through the sensor, causing the tank pressure to decrease. The compressor is switched off during the experiment to prevent refilling. The time required for the pressure to drop from 6 bar to 5 bar is recorded and used to estimate the airflow.

The analysis is based on the ideal gas law:

$$pV = nRT \tag{F.1}$$

(Dunlap et al., 2010)

where:

- p = absolute pressure (Pa)
- V = tank volume (m^3)
- n = amount of air (mol)
- R = gas constant
- T = absolute temperature (K)

Rewriting to obtain the molar flow rate:

$$\dot{n} = \frac{V}{RT} \times \dot{p} \tag{F.2}$$

Assuming constant temperature and converting to volumetric flow:

$$\dot{V}_{\text{air}} = \frac{V_{\text{tank}}}{P_{\text{amb}}} \cdot \dot{p} \tag{F.3}$$

where the ambient pressure during testing in Enschede was measured as $P_{\text{amb}} = 99{,}900$ Pa.

Using a finite difference approximation:

$$\dot{V}_{\text{air}} = \frac{V_{\text{tank}}}{P_{\text{amb}}} \cdot \frac{\Delta P_{\text{tank}}}{\Delta t} \tag{F.4}$$

This provides a direct relationship between pressure decay and airflow.

F.2.3 Results

Table F.1: Measured airflow under varying pressure and load conditions

Pressure (kPa)	Weight on system	Time (s) (6→5 bar)	$\dot{V}$ (m^3/s)	$\dot{V}$ (L/min)
3	0	8.85	0.005655	339.32
3	1000	13.19	0.003795	227.67
2	0	12.22	0.004096	245.74
2	1000	15.55	0.003219	193.12

G POSEIDON

***P**ressure-**O**utput for **S**ensing **E**xertion & **I**nfluence **D**ynamically **O**n **N**ormal-force*

G.1 Description

POSEIDON is based on the principle that two hydraulically coupled cylinders with equal fluid volume transmit force nearly one-to-one, neglecting fluid compressibility. The input cylinder is mounted at the robot's end effector, while the second, identical cylinder is used for sensing and actuation. Because the cylinders are fluid-bound, a force applied to the end-effector cylinder results in a corresponding displacement of the sensing cylinder.

The sensing cylinder is equipped with a linear potentiometer to measure its position. A DC motor is mechanically connected to this cylinder and generates a counteracting torque that is electronically linked to the potentiometer's displacement. This motor torque behaves as a virtual spring, continually attempting to return the cylinder to its neutral, fully decompressed position.

An equilibrium is reached when the external force applied to the end-effector cylinder is exactly balanced by the generated motor torque. The displacement at which this equilibrium occurs is linearly related to the applied external force.

The experimental setup is shown in figure G.1

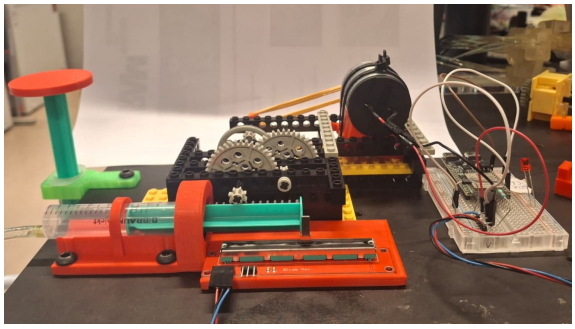


Figure G.1: POSEIDON

G.2 Result and Conclusion

The setup shown in Figure G.1 did not function as intended. The internal friction of the hydraulic cylinders proved to be substantially higher than anticipated. As a result, the soft LEGO axle used to mechanically couple the DC motor to the cylinder bent under load. This axle was required because a gear reduction was necessary. The DC motor alone was unable to generate sufficient torque. However, reinforcing the axle was not feasible, as the LEGO connections would fail and tear apart under higher forces.

A potential improvement would be to reduce the friction generated by the cylinders themselves; membrane-based cylinders could offer a promising alternative. Nonetheless, the goal of these proof-of-concept prototypes was to identify a viable working principle using the simplest possible implementation.

Given that this prototype is already more complex than both the ATLAS and AEOLUS concepts, and considering its unresolved mechanical limitations, further development of this approach has been discontinued. The core concept could not be sufficiently demonstrated, and the method is therefore considered unproven.

H Stakeholder Interview

At the start of this project, a prostate biopsy procedure was observed to gain a practical understanding of the clinical workflow. During this observation, questions were asked regarding the procedural nuances. These questions were asked to nurses with specialised experience in MRI-guided biopsies and a doctor present. The responses obtained are summarised below.

H.1 Indicators for Needle-Tumour Contact

- *Question: How do you know when you have reached the tumour? Can you feel when you enter tumour tissue?*

The doctor present reported that changes in tissue resistance can be felt during needle insertion. However, in current clinical practice for prostate biopsy, the Soteria (Bomers et al., 2017) is used to guide needle placement. This system provides precise information regarding the target depth, effectively eliminating reliance on tactile feedback. The nurses expressed full confidence in the system's measurements and used them to accurately position the needle. Breast biopsies are mostly done manually. Here, tactile feedback is more useful, but the MRI or ego guidance is still leading.

H.2 Misclassification of Tissue

- *Question: Since you can feel tumour tissue, are there other forms of tissue that are comparable?*

The doctor noted that certain tissues can mimic the sensation of a tumour, particularly in breast biopsies, where dense tissue or cysts may feel similar. Nevertheless, the placement of the needle does not rely solely on feeling; imaging modalities such as MRI or ultrasound serve as the primary guidance for targeting.

H.3 Desired Additional System Data

- *Question: When observing the Soteria System, what additional data would you like to receive from such a system?*

A key limitation identified with current robotic biopsy systems is the reliance on a pre-defined operational protocol without real-time feedback. Beyond MRI imaging, the system functions without awareness of its surrounding tissue, occasionally resulting in skipped steps. Nurses typically compensate for such deviations manually, which is suboptimal. The nurses stated that the skipping of steps mostly happens when the end effector is placed on the prostate, experiencing friction. Incorporating positional and force feedback could mitigate these issues, particularly when friction between the robot and the prostate occurs. Such feedback would indicate when the system is in contact with tissue or encountering resistance.

H.4 Failures and Mitigation

- *Question: What can go wrong during a prostate biopsy and how is this solved?*

Apart from the skipping issue, nurses indicated that the system may occasionally be unable to reach the intended target due to limitations in its operational range. This makes it unfeasible to take any biopsy since the MRI-guided biopsy is seen as the last resort. It is then up to the oncologist to make the countermeasures. However, such occurrences are infrequent and are not considered a major concern in clinical practice.

H.5 Overall Feedback

The nurses indicated that the Soteria system, while providing some advantages, remains suboptimal in its current form. Its primary perceived benefit is the reduction in physical effort, as operators no longer need to move as frequently during the procedure. However, the system exhibits limitations in positional accuracy, which can result in misplacement of the needle guide. These issues extend the duration of the procedure, with an average biopsy taking approximately one hour, which is longer than would be expected under optimal system performance.
During the observation of the biopsy procedures, it was noted that the nurses did not primarily rely on the system's measurements in millimetres. Instead, they tended to think in terms of the discrete "clicks" or steps of the robotic mechanism. This approach reflects experiential judgment rather than precise engineering accuracy, with nurses estimating the final position of the needle guide based on familiarity with the system's behaviour rather than exact metric data.

References

Automation, ATI Industrial (n.d.). *ATI Mini40 Force/Torque Sensor — Model Information*. https://www.ati-ia.com/products/ft/ft_models.aspx?id=mini40. Accessed: 2025-09-20.

Bomers, J. G. R. et al. (2017). 'Feasibility of a 2nd generation MR-compatible manipulator for transrectal prostate biopsy guidance'. In: *European Radiology* 27.4, pp. 1776–1782. DOI: 10.1007/s00330-016-4504-2.

Dunlap, Paul H. Jr. et al. (2010). *Pressure Decay Testing Methodology for Quantifying Leak Rates of Full-Scale Docking System Seals*. Tech. rep. NASA/TM–2010–216244. NASA Glenn Research Center. URL: https://ntrs.nasa.gov/api/citations/20100019164/downloads/20100019164.pdf.

Groenhuis, Vincent (2025). *Development and Control of Sunram/Mamri Robot Arm (MSc), available from 2026*. https://www.ram.eemcs.utwente.nl/education/assignments/development-and-control-sunrammamri-robot-arm-msc-available-2026. Accessed: 2025-10-01.

He, Binghan et al. (2024). 'Design and Control of a Compact Series Elastic Actuator Module for Robots in MRI Scanners'. In: *CoRR* abs/2406.07670. DOI: 10.48550/arXiv.2406.07670. arXiv: 2406.07670. URL: https://arxiv.org/abs/2406.07670.

International Society for Magnetic Resonance in Medicine (2025). *Understanding MRI Safety Labeling*. Accessed: 2025-09-30. URL: https://www.ismrm.org/smrt/safety_page/stoplight_20x30.pdf.

Leest, Marloes van der et al. (2019). 'Head-to-head comparison of transrectal ultrasound-guided prostate biopsy versus multiparametric prostate MRI with subsequent MRI-guided biopsy in biopsy-naïve men with elevated PSA: a large prospective multicenter clinical study'. In: *European Urology* 75.4, pp. 570–578. DOI: 10.1016/j.eururo.2018.11.023.

Lehmann, Thomas et al. (2017). 'Deflection Modeling for a Needle Actuated by Lateral Force and Axial Rotation During Insertion in Soft Phantom Tissue'. In: *Mechatronics* 44, pp. 120–132. DOI: 10.1016/j.mechatronics.2017.04.005.

Medical, Soteria (2024). *Remote Controlled Manipulator (RCM) for MRI-Guided Prostate Biopsy*. Accessed October 2025. URL: https://soteria-medical.com/product-information/remote-controlled-manipulator/.

Misra, Sarthak, Kyle B. Reed and Allison M. Okamura (2012). 'Steerable needles for minimally invasive medical procedures: A review'. In: *Medical Engineering & Physics* 34.6, pp. 745–756. DOI: 10.1016/j.medengphy.2012.02.014.

Moerman, Kevin M. et al. (2013). 'A novel MRI compatible soft tissue indentor and fibre Bragg grating force sensor'. In: *Medical Engineering & Physics* 35.4. Epub 2012 Jul 20, pp. 486–499. DOI: 10.1016/j.medengphy.2012.06.014. URL: https://pubmed.ncbi.nlm.nih.gov/22819569/.

Mühlenhoff, Julian, Oliver Radler and Thomas Sattel (2024). 'Development of a Hydraulic Actuator for MRI- and Radiation-Compatible Medical Applications'. In: *Actuators* 13.3, p. 90. DOI: 10.3390/act13030090. URL: https://www.mdpi.com/2076-0825/13/3/90.

Räuber, Sabine et al. (2025). 'Open-source, MRI-compatible grip force sensor for dynamic muscle imaging'. In: *MAGMA*. URL: https://www.sciencedirect.com/science/article/pii/S1350453312001701.

Rie, Jan Pieter de (2024). 'MR-Safe Needle Force Sensor: Enhancing Detection of Force and Elastomer Differentiation in Biopsy Procedures'. MA thesis. University of Twente.

URL: https://cloud.ram.eemcs.utwente.nl/index.php/s/XxDoWaQr4HeaNZp.

Robotics and Mechatronics (RaM), University of Twente (2025). *MR Safe Robotic Systems for Breast Biopsy*. https://www.ram.eemcs.utwente.nl/research/projects/mr-safe-robotic-systems-breast-biopsy. Accessed: 2025-09-10. URL: https://www.ram.eemcs.utwente.nl/research/projects/mr-safe-robotic-systems-breast-biopsy.

Schlabach, Paul (Sept. 2025). 'Pose Estimation of MRI-Compatible Biopsy Robot using Fiducials and Fiber Optic Stepper Motor Encoders'. Committee: Prof. Dr. Ir. S. Stramigioli, Dr. V. Groenhuis, Dr. Ir. W.M. Brink. MSc Assignment. Enschede, The Netherlands: University of Twente.

Ülgen, Nurettin, Dogangun Uzun and Özgür Koçaturk (2019). 'Phantom Study of a Fiber Optic Force Sensor Design for Biopsy Needles under MRI'. In: *Biomedical Optics Express* 10.1. Custom designed FPI sensor; range up to 13 N, resolution 0.1 N., pp. 242–251. DOI: 10.1364/BOE.10.000242. URL: https://www.osapublishing.org/boe/abstract.cfm?URI=boe-10-1-242.

UMC, Utrecht (2025). *Ultra High Field MRI: 7-Tesla*. Accessed: 30-09-2025. URL: https://www.umcutrecht.nl/en/ultra-high-field-mri-7-tesla.

UNC Health Johnston (2023). *MRI Breast and MRI Breast Biopsy*. https://www.unchealthjohnston.org/app/files/public/a2c73575-0e06-4bc9-9283-6f42adcacf0b/mri-breast-and-mri-breast-biopsy.pdf. Accessed: 2026-03-24.

Wu, Zicong et al. (2020). 'FBG-Based Triaxial Force Sensor Integrated with an Eccentrically Configured Imaging Probe for Endoluminal Optical Biopsy'. In: *arXiv preprint* arXiv:2006.06210. Submitted 11 Jun 2020; accuracy = 10.58 mN, 14.57 mN, 26.32 mN in X, Y, Z axes respectively. URL: https://arxiv.org/abs/2006.06210.